nature materials

ARTICLES

PUBLISHED ONLINE: 15 FEBRUARY 2016 | DOI: 10.1038/NMAT4569

Structured light enables biomimetic swimming and versatile locomotion of photoresponsive soft microrobots

Stefano Palagi[1], Andrew G. Mark[1], Shang Yik Reigh[2], Kai Melde[1], Tian Qiu[1,3], Hao Zeng[4], Camilla Parmeggiani[4,5], Daniele Martella[4], Alberto Sanchez-Castillo[1], Nadia Kapernaum[6], Frank Giesselmann[6], Diederik S. Wiersma[4], Eric Lauga[2] and Peer Fischer[1,6]*

Microorganisms move in challenging environments by periodic changes in body shape. In contrast, current artificial microrobots cannot actively deform, exhibiting at best passive bending under external fields. Here, by taking advantage of the wireless, scalable and spatiotemporally selective capabilities that light allows, we show that soft microrobots consisting of photoactive liquid-crystal elastomers can be driven by structured monochromatic light to perform sophisticated biomimetic motions. We realize continuum yet selectively addressable artificial microswimmers that generate travelling-wave motions to self-propel without external forces or torques, as well as microrobots capable of versatile locomotion behaviours on demand. Both theoretical predictions and experimental results confirm that multiple gaits, mimicking either symplectic or antiplectic metachrony of ciliate protozoa, can be achieved with single microswimmers. The principle of using structured light can be extended to other applications that require microscale actuation with sophisticated spatiotemporal coordination for advanced microrobotic technologies.

Mobile microscale robots might, in the future, navigate within the human body to perform minimally invasive diagnostic or therapeutic tasks[1,2]. Biological microorganisms represent the natural inspiration for this vision. For instance, microorganisms successfully swim and move through a variety of fluids and tissues. Locomotion in this regime, where viscous forces dominate over inertia (low Reynolds number), is possible only through non-reciprocal motions demanding spatiotemporal coordination of multiple actuators[3]. A variety of biological propulsion mechanisms at different scales, from the peristalsis of annelids (Fig. 1a) to the metachrony of ciliates (Fig. 1b), are based on the common principle of travelling waves (Fig. 1c). These emerge from the distributed and self-coordinated action of many independent molecular motors[4,5].

Implementing travelling-wave propulsion in an artificial device would require many discrete actuators, each individually addressed and powered in a coordinated fashion (Fig. 1d). The integration of actuators into microrobots that are mobile poses additional hurdles, because power and control need to be distributed without affecting the microrobots' mobility. Actuation of existing microrobots generally relies on applying external magnetic[6–10], electric[11] or optical[12] fields globally over the entire workspace. However, these approaches do not permit the spatial selectivity required to independently address individual actuators within a micro-device. Nevertheless, complex non-reciprocal motion patterns have been achieved by carefully engineering the response of different regions in a device to a spatially uniform external field[13,14]. The drawback is that this complicates the fabrication process, inhibits downscaling and constrains the device to a single predefined behaviour. These challenges mean that most artificial microrobots actually have no actuators. Rather, they are in most cases rigid monolithic structures, either pushed by chemical reactions[15] or directly manipulated by torques or forces applied by external magnetic fields[16–20]. Alternatively, they consist of flexible materials embedding, at best, a small number of passive degrees of freedom[21,22] (DOFs).

In macroscale robots, one approach to increase the number of DOFs has been to adopt soft bodies, capable of biomimetic actuation[23–28]. However, these approaches have resisted miniaturization. Soft active materials such as hydrogels[29] and liquid-crystal elastomers (LCEs), which exhibit stimuli-responsive behaviours, represent a potential route towards advanced biomimetic microrobots. At the microscale, soft active materials have enriched microrobots with additional functionalities, for example, on-demand drug release[30,31], and LCEs have recently actuated a walking microrobot[32]. Nevertheless, despite their soft bodies, these microrobots have each a unique function, predefined by its form, and few DOFs.

Here we present the use of structured light to power and control intrabody shape changes in microrobots. The technique enables fully artificial, self-propelled microswimmers. Indeed, they are true swimmers, because they move by deforming their soft body in a periodic way[4], and they do so with no forces or torques applied by external fields and no embedded biological cells. The versatility of the actuation mechanism allows a single device to execute a variety of gaits including propulsive motions that mimic the symplectic and antiplectic metachrony of ciliate protozoa. We

[1]Max Planck Institute for Intelligent Systems, 70569 Stuttgart, Germany. [2]Department of Applied Mathematics and Theoretical Physics, Centre for Mathematical Sciences, University of Cambridge, Cambridge CB3 0WA, UK. [3]Institute of Bioengineering, Ecole Polytechnique Fédérale de Lausanne (EPFL), CH-1015 Lausanne, Switzerland. [4]European Laboratory for Non Linear Spectroscopy (LENS), University of Florence, 50019 Sesto Fiorentino, Italy. [5]CNR-INO, 50019 Sesto Fiorentino, Italy. [6]Institut für Physikalische Chemie, Universität Stuttgart, 70569 Stuttgart, Germany. *e-mail: fischer@is.mpg.de

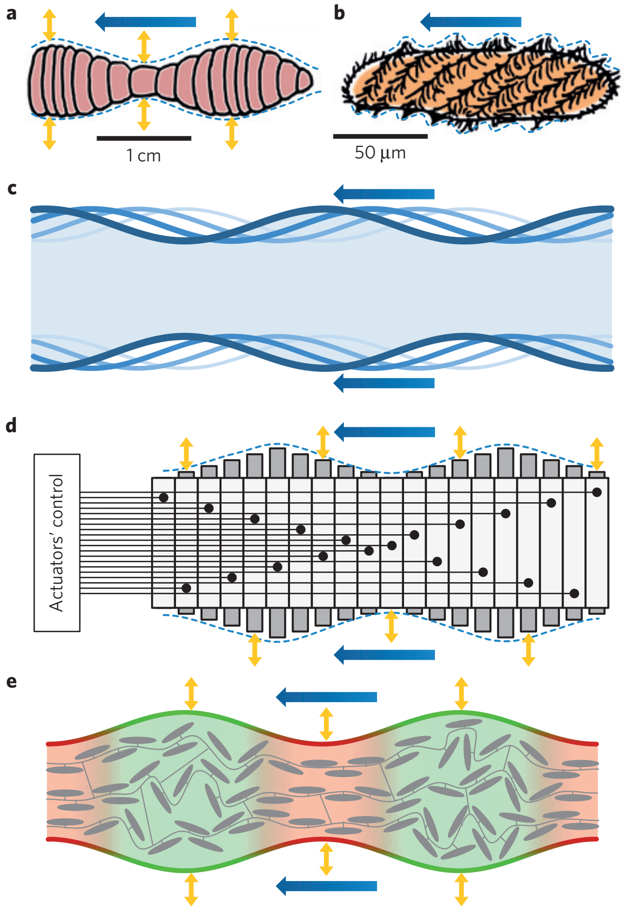

Figure 1 | Locomotion based on travelling-wave features, from nature to technology. a, Peristaltic locomotion of a worm by travelling waves of radial expansion and longitudinal contraction. **b**, Propulsion of a ciliate by metachronal waves emerging from the coordination of the cilia. **c**, Abstraction of the concept of travelling waves as a general locomotion principle. **d**, The artificial implementation of a travelling-wave propulsion would normally require the use of a large number of actuators that can be controlled in a precisely synchronized manner; this is unfeasible at the microscale. **e**, Concept of a selectively triggered continuous microrobot consisting of a soft active material.

describe the system as a new type of continuum actuator having a function-agnostic structure within which the light field can address a virtually unlimited number of DOFs (Fig. 1e). This versatility permits sophisticated and adaptable locomotion behaviours in submillimetre devices.

System concept

LCE materials exhibit a reversible shape change triggered by either heat or light[33,34]. As they can be fabricated at small length scales[35,36] and powered remotely, they are ideally suited for building mobile active robots with body sizes on the scale of hundreds of micrometres[32]. Instead of uniformly illuminating a complex, carefully engineered device[13] or focusing the light onto a single spot[37–39], our approach is to use structured dynamic light fields to excite sophisticated intrabody deformations within LCE microrobots with very simple and agnostic designs. In this scheme, the microrobot is regarded as a continuously addressable body that acts as an extended array of many infinitesimally small actuators, each of which can be independently triggered by the local light field. This makes the remote power, synchronization and control easily solved macroscale problems. It also has the benefit of transferring the burden of function from the microrobot's form into the light field, thereby simplifying its design and fabrication. Thus, rather than defining the microrobot's action once at the fabrication stage, it can be dynamically reconfigured in real time through software, with virtually limitless flexibility.

Selective deformation of soft continuous microscale bodies

We fabricate LCE microrobots in the form of long cylinders (about 1 mm in length and 200–300 μm in diameter), and flat discs (50 μm thick and either 200 or 400 μm in diameter) using the procedures reported in the Methods. At room temperature, the functional liquid-crystalline units (mesogens) possess orientational order, whose local direction and strength are described by the nematic director **n** and the order parameter Q (ref. 33). The photoresponse arises when the covalently bound azobenzene dye in the LCE absorbs the light, driving the elastomer through the nematic-to-isotropic phase transition. The mechanism consists of two different, but concurrent effects: the dye's *trans–cis* photoisomerization, and a light-induced thermal effect[32,33,37]. The axial nematic alignment of our cylinders leads, under homogeneous illumination, to axial contraction and simultaneous radial expansion (Fig. 2a). By small-angle X-ray scattering, we estimate a value for Q of 0.38 and axial contractions of about 30% (see Supplementary Information 4), corresponding to radial expansions of more than 18%. The elastomer formulations that we use possess two key characteristics: first, they do not require a second wavelength of light to excite relaxation after excitation; and they possess the fastest responses among LCEs (ref. 32), a prerequisite for the propulsion that we demonstrate[13,40].

Structured light fields are generated by an optical system based on a digital micromirror device (DMD) with $1{,}024 \times 768$ mirrors. The DMD spatially and temporally modulates the intensity of the laser light field that is projected into the microrobot workspace through a microscope objective (Fig. 2b; see Methods). Only those sections of the body that are illuminated are expected to deform, whereas the remainder will remain relaxed. Inspired by the locomotion of microorganisms, we implement travelling-wave body deformations with selectable wave parameters. We have simulated the response of the cylindrical microrobots to periodic patterns of light and dark stripes using a finite-element model (Fig. 2c,f; see Methods). The numerical simulations show that a localized decrease in the order parameter within the LCE material indeed results in a selective shape change. However, because of the material continuity conditions, binary illumination results in smooth transitions between the relaxed and deformed regions (Fig. 2c, simulation and 2d, experiment). The continuous actuator mimics, at microscopic scales, the action of the hydrostatic skeleton of worms during peristaltic motion, coupling radial and longitudinal deformation at constant volume.

Figure 2d shows a close-up side view of the experimental deformation of a cylindrical microrobot. A binary periodic light pattern, with a spatial wavelength of 260 μm, is projected onto the microrobot (radius of about 100 μm), leading to localized shape changes in the illuminated regions (see Methods and Supplementary Movie 1). Importantly, neither relaxation nor spreading of the deformation due to heat transfer is observed, rather the shape changes are localized and stable. The light absorption profile through the material results in stronger illumination and heating of the surface that faces the light source compared with the opposite surface. However, so long as the temperature and illumination are sufficient to drive the response above the critical point and into saturation (see Supplementary Fig. 4), there is no strong differential deformation between the upper and lower surfaces.

The dynamic behaviour of a microrobot (length of 1.3 mm and radius of 170 μm) is shown by the sequence of frames in Fig. 2e, imaged from the top. A binary periodic light field (shown as the green overlay), travelling from left to right at a frequency of 1 Hz, is projected onto the microrobot, which is anchored to the

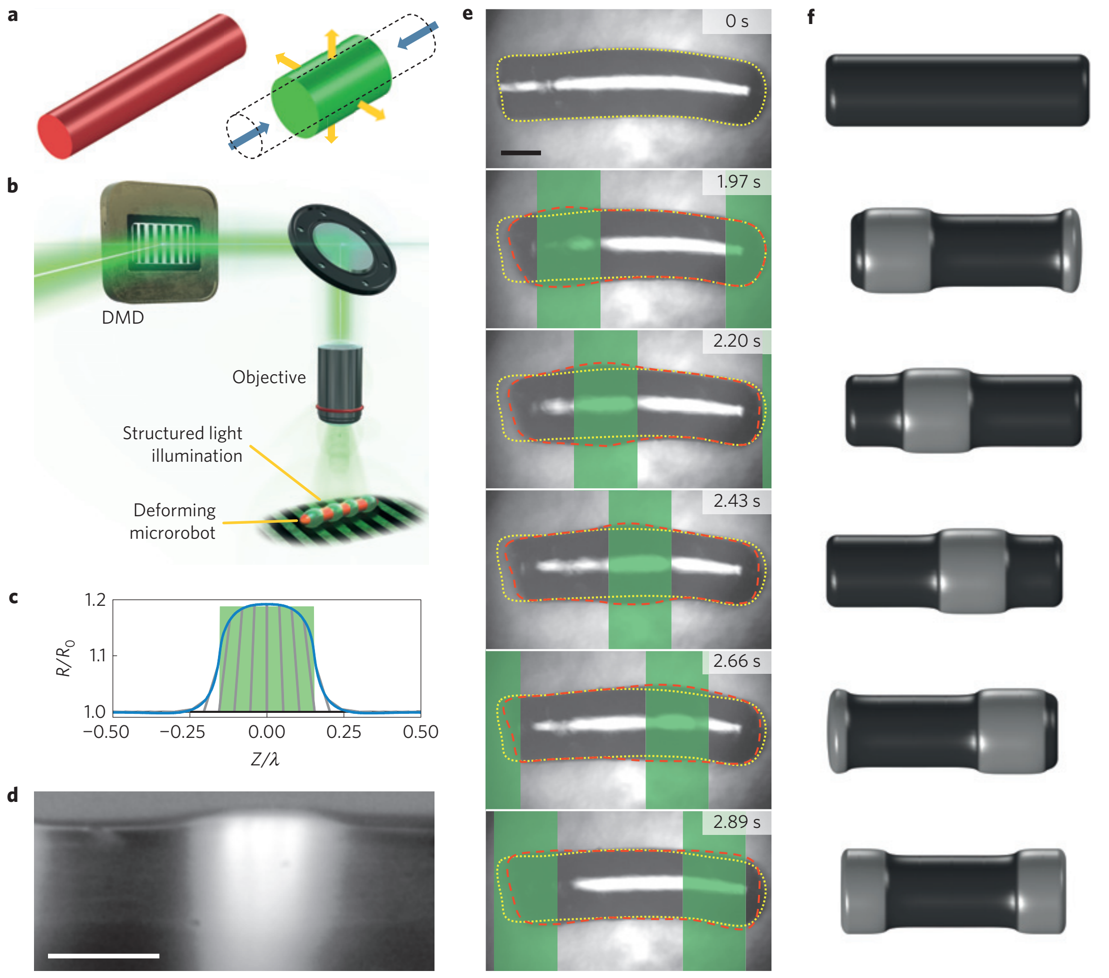

Figure 2 | Deformation of microrobots made of soft active materials wirelessly controlled by dynamic light fields. a, Finite-element simulation of a cylindrical microrobot (length = 1 mm, diameter = 200 μm) at rest (left) and after full deformation (right, emphasized by a 2× factor). The blue and yellow arrows represent the axial contraction and radial expansion, respectively. **b**, Concept and main elements of the system. The DMD modulates the incoming light beam in both space and time. The microscope objective projects the dynamic light field onto the soft microrobot, which deforms in a selective fashion. **c**, Results from finite-element simulation showing normalized radius (a/a_0) as a function of axial position normalized to wavelength (Z/λ) in response to localized illumination (green): rest configuration (black) and deformed profile (blue). Owing to incompressibility of the material, the discontinuous pattern of illumination results in a continuous, smooth profile of deformation, and longitudinal displacement of the surface elements (grey lines). **d**, High-resolution experimental side-view image of the selective deformation of a microrobot confined to the area of illumination. Scale bar, 100 μm. **e**, Experimental top-view images showing the deformation of an anchored cylindrical microrobot under a periodic light pattern travelling from left to right (illuminated area represented by the green overlay; first frame and yellow dotted line: rest configuration; red dashed line: deformed profile). Scale bar, 200 μm. **f**, Corresponding simulations of the behaviour of the microrobot.

lower surface. The portions of the device that are illuminated expand transversely, and follow the projected pattern as it travels along the body (see Supplementary Movie 1). For comparison, Fig. 2f shows the results from the corresponding numerical simulation. Hence, it is possible to locally address and power an extended continuous actuator system using light, and thus obtain complex coordinated motion behaviours such as biomimetic travelling-wave deformations. Waves not only mimic the behaviours that many small organisms use for propulsion, but have the benefit of abstracting a theoretically infinite number of intrinsic DOFs down to a handful of easily recognized parameters.

Self-propelled biomimetic microswimmers

We exploit these travelling-wave shape changes to achieve fully artificial self-propelled microswimmers. Like biological microswimmers, these microrobots propel themselves through periodic body deformations[4], which are generated neither by externally applied forces or torques, nor by embedded biological cells.

Figure 3a shows how a fiducial point on the top surface of a microrobot moves in the body frame in response to a light-induced travelling wave that moves from right to left. Over one cycle, the point describes an anticlockwise loop, deforming radially by ±5 μm at the peak and trough of the passing illumination. It also moves longitudinally owing to the contraction of its neighbouring regions. The trajectory calculated on the basis of the measured order parameter and assuming sinusoidal wave deformation (yellow, see Supplementary Information 9) is in substantial agreement with the experimental one. The important characteristic for swimming is that, because of the material properties of the soft actuator, any point on the surface of the body describes an open orbit, meaning that its trajectory is non-reciprocal.

Figure 3c illustrates the movement of a microrobot (length of 1,230 μm, radius of 120 μm) freely suspended in a fluid and undergoing travelling-wave deformations. The microrobot is suspended within a viscous glycerol–water solution far from any solid boundary (see Methods), and a periodic binary light pattern

NATURE MATERIALS DOI: 10.1038/NMAT4569

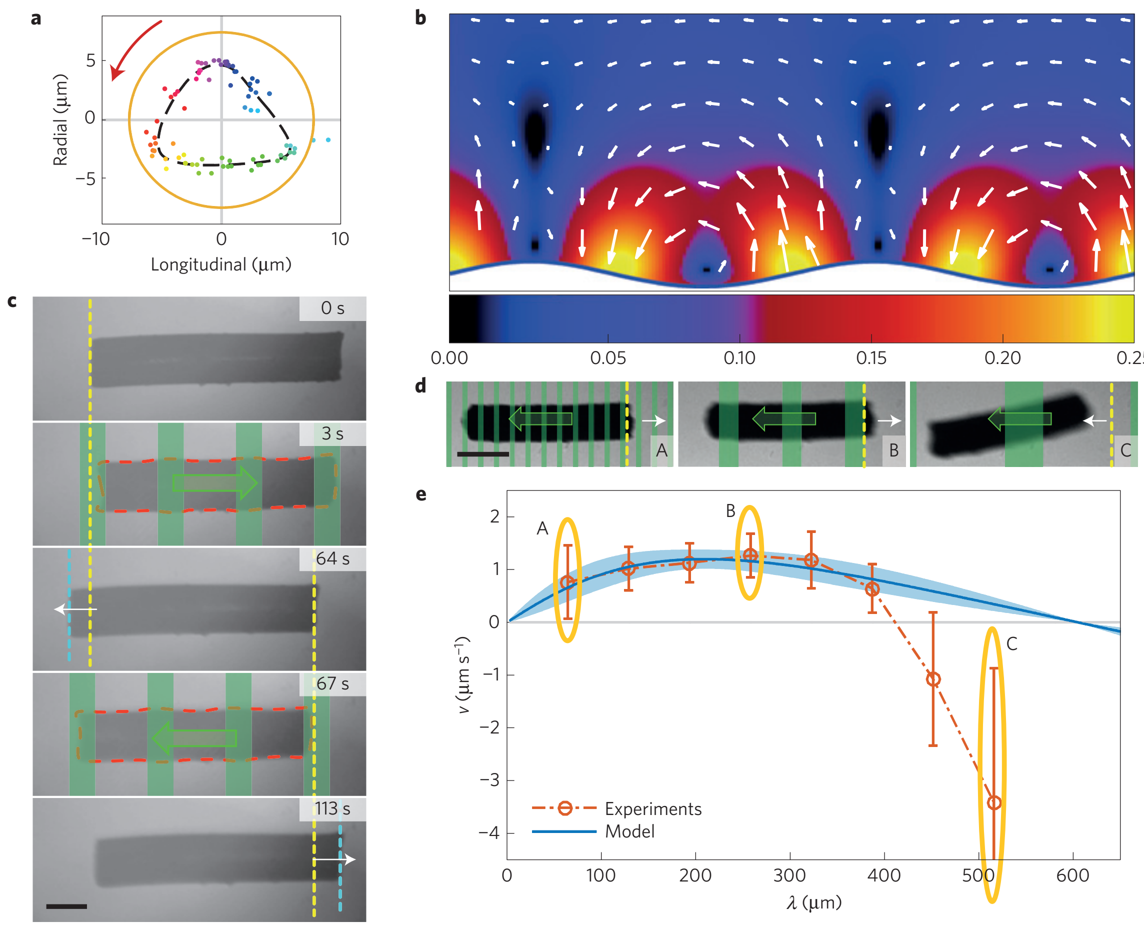

Figure 3 | Force- and torque-free swimming of a cylindrical microrobot driven by light-controlled travelling-wave deformations. a, Trajectory of a fiducial point on the surface of a 100-μm-diameter cylindrical microrobot exposed to a periodic travelling light pattern (frequency, $f=1$ Hz; duty cycle, $dc=1/3$). Over one cycle, the point displaces radially and longitudinally in response to the passing light field. The colour progression (indicated by the red arrow) represents different phases within the cycle. The yellow line represents a calculated trajectory based on the measured order parameter for the same microrobot radius and deformation wavelength, assuming a sinusoidal wave. **b**, Instantaneous fluid velocity field induced by the deformation of a cylindrical microrobot in the body frame of the cylinder from the analytical theory. The colour map shows the magnitudes of the fluid velocity v scaled by the wave velocity U, that is, v/U. The white arrows indicate the direction of the fluid flow. The wave travels from the right to the left. **c**, Back and forth swimming of a cylindrical microrobot propelled by travelling-wave deformations (red dashed line: deformed profile). The green overlays and arrows represent the periodic light pattern and its travelling direction, respectively. Yellow and cyan dashed lines represent the initial and final position of the leading edge of the microswimmer, respectively. **d**, Displacements of a microrobot (yellow dashed line: reference position) when travelling light patterns having different wavelengths (green overlays, direction according to green arrows) are applied. The swimming direction (white arrows) is opposite to the patterns' travelling direction for short wavelengths, but is the same for longer ones. **e**, Velocity (red circles and dash-dot line; average over 8 independent measurements, error bars: standard deviation), along with the analytical model (blue solid line; light blue area: 95% confidence interval, wave amplitude b and wavelength constant λ_c estimated by fitting over experimental data). The three encircled measurements refer to the three images in **d**. Scale bars, 200 μm.

(pattern wavelength $\lambda = 387$ μm, frequency $f = 2$ Hz, shown as a green overlay) is projected onto it to drive wave deformations along its length. The body undergoes a net displacement of 110 μm at a speed of 2.1 μm s^{-1} in the direction opposite to that of the wave. Switching the direction of the moving light pattern reverses the swimming direction. Moving backwards, the microrobot displaces about 120 μm at a speed of 2.8 μm s^{-1} (see Supplementary Movie 2). The current propulsion performance can be enhanced by improving the active response of the soft materials. For instance, a lower transition temperature leads to a faster response in the fluid. Moreover, an improved order parameter enables larger deformation amplitudes.

Distinct from the case of manipulation by magnetic fields, the external light field only provides power and permits control of the microrobots. The driving actions are generated by the light-triggered molecular reorientation within the soft active material, so that the microrobots' propulsion is fully remotely controllable.

The self-propulsion of the cylindrical microrobot by travelling-wave motions closely mimics the propulsion of microscopic biological swimmers[4], particularly ciliates (for example, *Paramecium*) that self-propel using metachronal waves. Here, the directed motion of periodic light patterns drives deformation waves along the cylinder, thereby dragging the surrounding fluid. Propulsion, generally in the direction opposite to the waves, arises because the net hydrodynamic force on the cylinder must be zero. An analysis similar to that first developed in refs 41,42 can be applied to the current geometry, with details shown in Supplementary Information 9. Considering an infinitely long cylinder of radius a undergoing sinusoidal radial deformation of amplitude $b \ll a$, wavelength λ and frequency f, and assuming the cylinder to be incompressible, we predict the body's propulsion velocity V to be

$$V = \frac{(2\pi b)^2 f}{\lambda} G\left(\frac{2\pi a}{\lambda}\right) \quad (1)$$

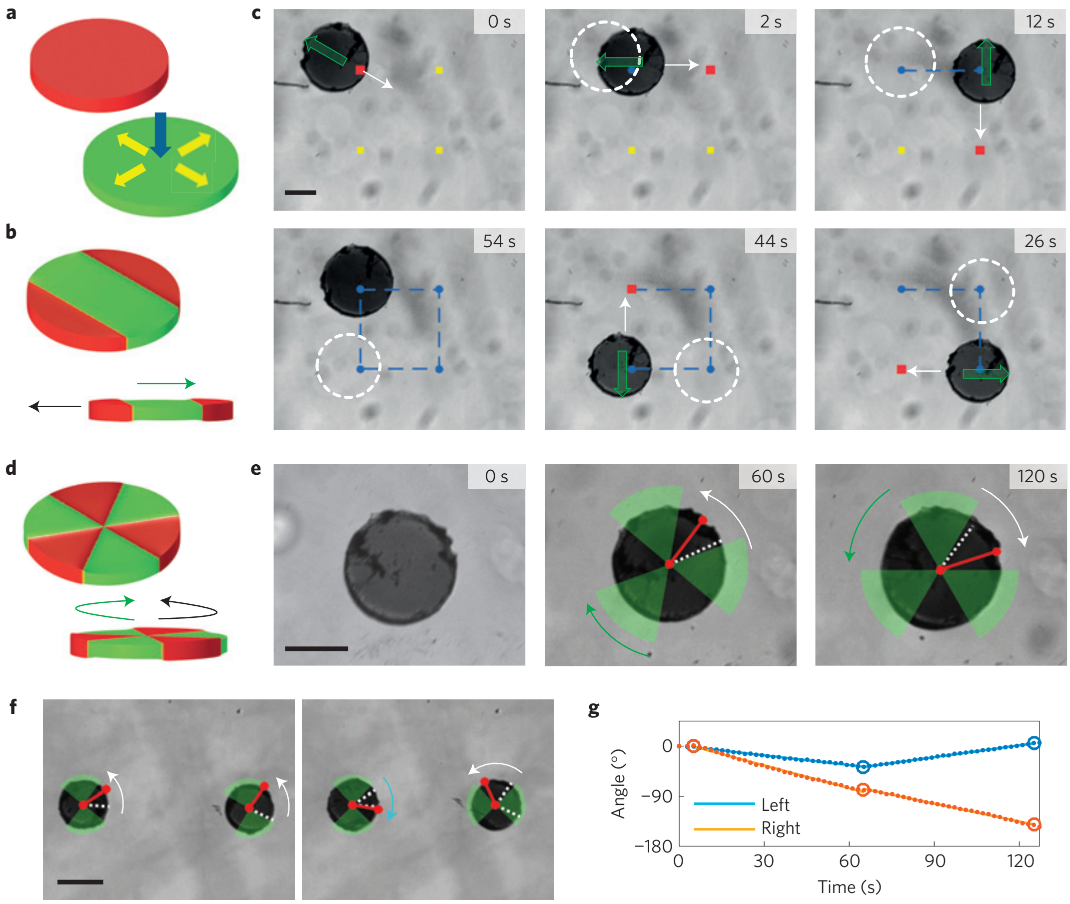

Figure 4 | In-plane controlled locomotion of disc-shaped microrobots. The symmetry of the disc means that several different deformation behaviours can be implemented by the appropriate light fields. **a**, Finite-element simulation of uniform deformation: thickness contraction (blue arrow) and in-plane expansion (yellow arrows). Initial diameter, 400 μm; initial thickness, 50 μm. **b**,**c**, Translational locomotion by plane travelling waves. **b**, Simulated deformation of a disc under a plane-wave light field (wavelength 400 μm); green arrow, travelling-wave direction; black arrow, expected translation. The disc's symmetry permits motion in every in-plane direction. **c**, Two-dimensional translational locomotion along a square path by plane-wave light patterns travelling in different directions. The green arrows indicate the travelling wave direction, and white arrows the disc's direction of travel to the next waypoint (red). The disc's previous position is outlined in dashed white, and the completed track in dashed blue. The microrobot does not rotate at the vertices, but only changes its course. **d**,**e**, In-place rotation by azimuthal travelling waves. **d**, Simulated deformation of a disc under an azimuthal-wave light field; green arrow: travelling-wave direction; black arrow: expected microrobot rotation. **e**, In-place rotation of the same microrobot driven by azimuthal-wave light patterns (green overlays) rotating in different directions (green arrows) relative to a reference orientation (dashed line). **f**,**g**, Parallel independent control of multiple microrobots by local light patterns. **f**, First, two azimuthal-wave light patterns (green overlays) rotating in the same direction are applied, driving the concordant rotation of the microrobots (white arrows). Then the rotation direction of the left microrobot is changed (cyan arrow) by reversing the direction of the driving local light field. **g**, Resulting angle of the two microrobots. Scale bars, 200 μm.

where the function G is given by

$$G(x)=\frac{1}{2}\left[\frac{\left(1+(2/x)^2\right)K_1^2(x)-K_0^2(x)}{K_0^2(x)-K_1^2(x)+(2/x)K_0(x)K_1(x)}-\left(\frac{2}{x}\right)^2\right] \qquad (2)$$

with K_i being the modified Bessel function of the second kind ($i=0,1$). The predicted fluid velocity field near the swimmer is shown in Fig. 3b, as observed in the body frame.

According to the numerical simulations and experimental results reported in Fig. 2c,d, the deformation profile is smoother than the applied illumination profile, because of the finite elasticity of the LCE. For this reason, the amplitude of the wave deformation b exhibits a wavelength dependence, which we describe by the following empirical relationship

$$b=b_0\left(1-\mathrm{e}^{-\frac{\lambda}{\lambda_c}}\right) \qquad (3)$$

where b_0 is the maximum amplitude of deformation, which occurs at long wavelengths, and λ_c is the critical wavelength below which the deformation amplitude is attenuated (see Supplementary Information 7 and 8). In particular, a lower value of λ_c implies a lower smoothing effect and an improved ability of the microswimmer to execute deformations with narrow spatial features. Moreover, the linear dependence of the swimming speed on the frequency of actuation reported in (1) is valid only for relatively low frequencies, limited by the characteristic time of the material response (see Supplementary Information 10). Nonetheless, for the swimming experiment reported above, the model predicts a swimming speed of 2.6 μm s^{-1}, in very good agreement with the measured speed of 2.1–2.8 μm s^{-1}.

Equation (1) predicts a dependence of the swimming velocity on the deformation wavelength. We investigated this dependence by driving another microrobot (length of 680 μm, radius of 75 μm) with patterns of various wavelengths (shown as green overlays in Fig. 3d) and compared its speed with the model's predictions (Fig. 3e; see Methods). Notably, this analysis is possible only because in our scheme deformation parameters such as the wavelength are not pre-programmed in the swimmer's structure, but can be arbitrarily controlled by the applied light field.

The most striking feature is the counterintuitive retrograde swimming that occurs without wave reversal at long wavelengths. This arises because the amplitude of the longitudinal deformation increases with wavelength, thus changing its importance relative to the radial expansion. The microswimmer therefore exhibits two different swimming modes, one 'positive' and one 'negative', dominated by the radial and longitudinal deformations, respectively. We observe the transition between the two modes at shorter wavelengths (>425 μm) than predicted by the model (>600 μm). This is most likely because the theory models an infinitely long swimmer. For our finite-length swimmer, the effects of truncation become more pronounced at long wavelengths as λ approaches the length of the swimmer.

The positive swimming mode observed at short wavelengths closely mimics the symplectic metachrony executed by many ciliate protozoa[43]. In this mode, the metachronal wave travels in the same direction as the cilia's power stroke, opposite to the swimming direction. Other ciliates use antiplectic metachrony in which the wave and the swimming directions are the same. As the sense of the orbit described by a surface point (see Fig. 3a) does not reverse with respect to the travelling wave, our negative mode mimics antiplectic metachrony by changing the relative amplitude of the longitudinal versus axial deformation, rather than by reversal of the relative phase[44] (see Supplementary Information 9). This pseudo-antiplectic behaviour is an unusual mode, predicted by classical models but so far not seen in nature. True antiplectic metachrony could be achieved by constructing the swimmer's body from an auxetic (negative Poisson's ratio) material. Passive, microscale auxetic metamaterials have been fabricated using technology that can be applied to LCEs (refs 45,46). Nevertheless, our microswimmers are capable of broader functionality than is found in nature, where any given species of ciliate exhibits only one mode of metachrony.

Equation (1) suggests that the swimming speed will scale favourably as the swimmers are made smaller. The frequency is limited by the material response time; as this is a thermally driven process it is expected to scale inversely with system size, with smaller structures heating more rapidly. Similarly, the finite-element results in Supplementary Information 8 indicate that the critical wavelength λ_c scales linearly with swimmer radius, so smaller structures are capable of deforming with smaller wavelengths. On the other hand, because it is essentially a strain, the maximum radial deformation scales linearly with radius, and shrinks with the size of the structure. The net result is that V is expected to remain unchanged with body size.

Versatile microrobot locomotion on demand

We also fabricated microrobots by photolithographically patterning discs (400 μm in diameter and 50 μm thick) where the nematic director **n** is oriented perpendicular to the disc's surface. These simple structures undergo thickness compression accompanied by in-plane expansion (Fig. 4a). The nematic LCE used for these discs exhibits typical contractions of about 20% (ref. 32). Crucially, their axial symmetry means that, within the disc's plane, there is no preferential direction of movement. Thus, the disc's course can be controlled in two dimensions by the direction of the induced wave deformations (Fig. 4b).

The disc microrobots are immersed in silicone oil, close to the bottom of the container, and oriented so that the light patterns are projected onto their face (see Methods). We direct the locomotion of a disc microrobot along a two-dimensional 500 μm square path (Fig. 4c and Supplementary Movie 3). The microrobot's position is automatically tracked by closed-loop control software and directed to the next waypoint (red squares) by the proper travelling-wave pattern. The direction of motion (white arrows) is opposite to the travelling-wave direction (green arrows). The average speed of the microrobot along the path is about 40 μm s^{-1}, which corresponds to about 0.1 bodylengths s^{-1}. Supplementary Movie 3 also shows the microrobot being guided along a different, diamond-shaped path. The microrobot does not rotate at the vertices, but only changes its course according to the applied light pattern.

The high symmetry of the discs means that these microrobots offer the possibility of new deformation behaviours in addition to linear waves. This can be used to generate alternative gaits. As an example, we project rotating fan-shaped light fields as azimuthal travelling waves ($\lambda = 2\pi/3$ rad, $f = 3$ Hz) centred on the very same microrobot (Fig. 4d,e). This generates controlled rotation without translation (see Supplementary Movie 3) with a rotation speed of about 0.5° s^{-1}.

The high spatial selectively of light fields can also enable the independent control of multiple microrobots at once[47]. Here we simultaneously control two smaller disc-shaped microrobots (diameter: 200 μm; thickness: 50 μm) executing a rotation stroke (Supplementary Movie 4 and Fig. 4f). Fan-shaped rotating light patterns ($\lambda = \pi$ rad, $f = 3$ Hz, shown as green overlays) are projected onto each of the two microrobots. First, the two light patterns are both rotated clockwise, so that both of the discs rotate anticlockwise (white arrows in Fig. 4f left). Then, the left microrobot's sense of rotation is reversed (cyan arrow in Fig. 4f right), whereas the right one continues to rotate anticlockwise (white arrow in Fig. 4f right). The average absolute rotation speed is about 1° s^{-1}. Independent control over the rotation of the two microrobots is thus achieved.

The disc microrobots demonstrate that a single microrobot can be directed to execute internal wave-like deformations with a variety of frequencies, wavelengths and symmetries, which in turn drive a number of different whole-body gaits. For the motions shown here, we estimate that traditional schemes would require approximately 100 actuators to be embedded, individually controlled and macroscopically coordinated within a 400-μm-diameter untethered device to obtain the same spatial resolution of actuation achieved in the current implementation.

Outlook

In summary, structured light fields allow us to exercise low-level control over the local actuation dynamics within the body of microrobots made of soft active materials. This in turn enables the high-level control over the microrobots' macroscopic behaviour, such as locomotion, with a level of versatility that is unmatched in microscale robotics. Even though a light-based approach requires optical access, which may limit the range of applications, such access is a natural prerequisite in any scheme that requires visualization. Moreover, although here we focus on bioinspired travelling waves, our approach is not limited to wave-like motions. In fact, more complex behaviours can easily be achieved by simply conceiving the proper structured light fields. Our subject here was generating sophisticated functions from simple robots by structured light fields, but even more powerful and exotic behaviours can be expected when complicated fields are combined with intrinsically functional microrobot designs[48]. Although we have focused on metachronal waves used by ciliates, it should be noted that nematodes, whose size is comparable to our swimmers, swim by another propulsion mechanism: undulation[49]. The implementation of undulation is in principle possible with the system we describe, but would require a modified fabrication procedure for the swimmers. The level of control that we demonstrate represents an essential step towards sophisticated microrobotic technologies and advanced microrobotic applications.

Methods

Methods and any associated references are available in the online version of the paper.

Received 17 November 2015; accepted 18 January 2016;
published online 15 February 2016

References

1. Nelson, B. J., Kaliakatsos, I. K. & Abbott, J. J. Microrobots for minimally invasive medicine. *Annu. Rev. Biomed. Eng.* **12,** 55–85 (2010).
2. Sitti, M. *et al*. Biomedical applications of untethered mobile milli/microrobots. *Proc. IEEE* **103,** 205–224 (2015).
3. Purcell, E. M. Life at low Reynolds number. *Am. J. Phys.* **45,** 3–11 (1977).
4. Lauga, E. & Powers, T. R. The hydrodynamics of swimming microorganisms. *Rep. Prog. Phys.* **72,** 96601 (2009).
5. Elgeti, J. & Gompper, G. Emergence of metachronal waves in cilia arrays. *Proc. Natl Acad. Sci. USA* **110,** 4470–4475 (2013).
6. Choi, H. *et al*. Two-dimensional locomotion of a microrobot with a novel stationary electromagnetic actuation system. *Smart Mater. Struct.* **18,** 115017 (2009).
7. Kummer, M. P. *et al*. OctoMag: an electromagnetic system for 5-DOF wireless micromanipulation. *IEEE Trans. Robot.* **26,** 1006–1017 (2010).
8. Fischer, P. & Ghosh, A. Magnetically actuated propulsion at low Reynolds numbers: towards nanoscale control. *Nanoscale* **3,** 557–563 (2011).
9. Palagi, S., Mazzolai, B., Innocenti, C., Sangregorio, C. & Beccai, L. How does buoyancy of hydrogel microrobots affect their magnetic propulsion in liquids? *Appl. Phys. Lett.* **102,** 124102–124105 (2013).
10. Shields, A. R. *et al*. Biomimetic cilia arrays generate simultaneous pumping and mixing regimes. *Proc. Natl Acad. Sci. USA* **107,** 15670–15675 (2010).
11. Donald, B. R., Levey, C. G., McGray, C. D., Paprotny, I. & Rus, D. An untethered, electrostatic, globally controllable MEMS micro-robot. *J. Microelectromech. Syst.* **15,** 1–15 (2006).
12. Hu, W., Ishii, K. S. & Ohta, A. T. Micro-assembly using optically controlled bubble microrobots. *Appl. Phys. Lett.* **99,** 94103 (2011).
13. van Oosten, C. L., Bastiaansen, C. W. M. & Broer, D. J. Printed artificial cilia from liquid-crystal network actuators modularly driven by light. *Nature Mater.* **8,** 677–682 (2009).
14. Diller, E., Zhuang, J., Zhan Lum, G., Edwards, M. R. & Sitti, M. Continuously distributed magnetization profile for millimeter-scale elastomeric undulatory swimming. *Appl. Phys. Lett.* **104,** 174101 (2014).
15. Sánchez, S., Soler, L. & Katuri, J. Chemically powered micro- and nanomotors. *Angew. Chem. Int. Ed.* **54,** 1414–1444 (2015).
16. Schamel, D. *et al*. Nanopropellers and their actuation in complex viscoelastic media. *ACS Nano* **8,** 8794–8801 (2014).
17. Iacovacci, V. *et al*. Untethered magnetic millirobot for targeted drug delivery. *Biomed. Microdevices* **17,** 1–12 (2015).
18. Servant, A., Qiu, F., Mazza, M., Kostarelos, K. & Nelson, B. J. Controlled *in vivo* swimming of a swarm of bacteria-like microrobotic flagella. *Adv. Mater.* **27,** 2981–2988 (2015).
19. Snezhko, A., Belkin, M., Aranson, I. S. & Kwok, W. K. Self-assembled magnetic surface swimmers. *Phys. Rev. Lett.* **102,** 118103 (2009).
20. Snezhko, A. & Aranson, I. S. Magnetic manipulation of self-assembled colloidal asters. *Nature Mater.* **10,** 698–703 (2011).
21. Dreyfus, R. *et al*. Microscopic artificial swimmers. *Nature* **437,** 862–865 (2005).
22. Qiu, T. *et al*. Swimming by reciprocal motion at low Reynolds number. *Nature Commun.* **5,** 5119 (2014).
23. Majidi, C. Soft robotics: a perspective—current trends and prospects for the future. *Soft Robot.* **1,** 5–11 (2013).
24. Kim, S., Laschi, C. & Trimmer, B. Soft robotics: a bioinspired evolution in robotics. *Trends Biotechnol.* **31,** 287–294 (2013).
25. Laschi, C. & Cianchetti, M. Soft robotics: new perspectives for robot bodyware and control. *Front. Bioeng. Biotechnol.* **2,** 3 (2014).
26. Rus, D. & Tolley, M. T. Design, fabrication and control of soft robots. *Nature* **521,** 467–475 (2015).
27. Ranzani, T., Gerboni, G., Cianchetti, M. & Menciassi, A. A bioinspired soft manipulator for minimally invasive surgery. *Bioinspir. Biomim.* **10,** 035008 (2015).
28. Bartlett, N. W. *et al*. A 3D-printed, functionally graded soft robot powered by combustion. *Science* **349,** 161–165 (2015).
29. Hauser, A. W., Evans, A. A., Na, J.-H. & Hayward, R. C. Photothermally reprogrammable buckling of nanocomposite gel sheets. *Angew. Chem. Int. Ed.* **54,** 5434–5437 (2015).
30. Tabatabaei, S. N., Lapointe, J. & Martel, S. Shrinkable hydrogel-based magnetic microrobots for interventions in the vascular network. *Adv. Robot.* **25,** 1049–1067 (2011).
31. Fusco, S. *et al*. An integrated microrobotic platform for on-demand, targeted therapeutic interventions. *Adv. Mater.* **26,** 952–957 (2014).
32. Zeng, H. *et al*. Light-fueled microscopic walkers. *Adv. Mater.* **27,** 3883–3887 (2015).
33. Warner, M. & Terentjev, E. M. *Liquid Crystal Elastomers* Vol. 120 (Oxford Univ. Press, 2003).
34. Ohm, C., Brehmer, M. & Zentel, R. Liquid crystalline elastomers as actuators and sensors. *Adv. Mater.* **22,** 3366–3387 (2010).
35. Fleischmann, E.-K. *et al*. One-piece micropumps from liquid crystalline core-shell particles. *Nature Commun.* **3,** 1178 (2012).
36. Fleischmann, E.-K., Forst, F. R. & Zentel, R. Liquid-crystalline elastomer fibers prepared in a microfluidic device. *Macromol. Chem. Phys.* **215,** 1004–1011 (2014).
37. Camacho-Lopez, M., Finkelmann, H., Palffy-Muhoray, P. & Shelley, M. Fast liquid-crystal elastomer swims into the dark. *Nature Mater.* **3,** 307–310 (2004).
38. Wang, L. *et al*. A bioinspired swimming and walking hydrogel driven by light-controlled local density. *Adv. Sci.* **2,** 1500084 (2015).
39. Uchida, E., Azumi, R. & Norikane, Y. Light-induced crawling of crystals on a glass surface. *Nature Commun.* **6,** 7310 (2015).
40. Khatavkar, V. V., Anderson, P. D., den Toonder, J. M. J. & Meijer, H. E. H. Active micromixer based on artificial cilia. *Phys. Fluids* **19,** 083605 (2007).
41. Taylor, G. Analysis of the swimming of microscopic organisms. *Proc. R. Soc. Lond. A* **209,** 447–461 (1951).
42. Taylor, G. The action of waving cylindrical tails in propelling microscopic organisms. *Proc. R. Soc. Lond. A* **211,** 225–239 (1952).
43. Knight-Jones, E. W. Relations between metachronism and the direction of ciliary beat in Metazoa. *J. Cell Sci.* **s3-95,** 503–521 (1954).
44. Childress, S. *Mechanics of Swimming and Flying* Vol. 2 (Cambridge Univ. Press, 1981).
45. Bückmann, T. *et al*. Tailored 3D mechanical metamaterials made by dip-in direct-laser-writing optical lithography. *Adv. Mater.* **24,** 2710–2714 (2012).
46. Zeng, H. *et al*. High-resolution 3D direct laser writing for liquid-crystalline elastomer microstructures. *Adv. Mater.* **26,** 2319–2322 (2014).
47. Hu, W., Fan, Q. & Ohta, A. Interactive actuation of multiple opto-thermocapillary flow-addressed bubble microrobots. *Robot. Biomimetics* **1,** 14 (2014).
48. White, T. J. & Broer, D. J. Programmable and adaptive mechanics with liquid crystal polymer networks and elastomers. *Nature Mater.* **14,** 1087–1098 (2015).
49. Berman, R. S., Kenneth, O., Sznitman, J. & Leshansky, A. M. Undulatory locomotion of finite filaments: lessons from Caenorhabditis elegans. *New J. Phys.* **15,** 075022 (2013).

Acknowledgements

This work was in part supported by the European Research Council under the ERC Grant agreements 278213 and 291349, and the DFG as part of the project SPP 1726 (microswimmers, FI 1966/1-1). S.P. acknowledges support by the Max Planck ETH Center for Learning Systems. We thank A. Posada for help with the movies and figures.

Author contributions

S.P., A.G.M. and P.F. proposed the experiment; S.P., A.G.M. and K.M. built the structured light set-up; H.Z., C.P., D.M. and D.S.W. synthesized the LCE and formed the cylindrical samples; S.P. performed the experiments and numerical simulations; S.P. and T.Q. fabricated the disc by photolithography; S.P., A.G.M., A.S.-C., N.K. and F.G. characterized the LCE material by SAXS; S.Y.R. and E.L. developed the analytical theory model; S.P., A.G.M. and P.F. wrote the manuscript with contributions from all authors.

Additional information

Supplementary information is available in the online version of the paper. Reprints and permissions information is available online at www.nature.com/reprints. Correspondence and requests for materials should be addressed to P.F.

Competing financial interests

The authors declare no competing financial interests.

NATURE MATERIALS DOI: 10.1038/NMAT4569

Methods

Fabrication of the microrobots. The microrobots consist of nematic LCEs based on either the side-on mesogen M1 (cylindrical microrobots) or the end-on mesogen M2 (disc microrobots), and containing a custom azobenzene dye (mesogens and dye synthesized following previously reported procedures, see Supplementary Information 3).

For the cylinders, a mixture is prepared with 85 mol% of mesogen M1, 13 mol% of crosslinker CL1, 1 mol% initiator and 1 mol% azo dye. A drop of the mixture is placed on a glass slide and heated to the isotropic phase ($T > 80\,^{\circ}$C). It is then allowed to cool until it becomes viscous enough to pull a continuous fibre using a fine tip. The fibre is cured with an ultraviolet lamp during pulling, and then cut with a scalpel into 1-mm-long cylinders.

For the discs, a mixture is prepared with 77 mol% of mesogen M2, 20 mol% of crosslinker CL2, 2 mol% initiator and 1 mol% azo dye. The mixture is infiltrated into a glass cell at 80 °C, and then slowly cooled to room temperature. The cell consists of two glass slides, cleaned by Ar plasma, separated by 50 μm spacers. The mixture is then ultraviolet-cured through a photo-mask by a mask aligner (MJB4, SUSS MicroTec) to obtain discs with diameters of either 200 or 400 μm. Once the cell is opened, the discs are manually detached from the substrate with a razor blade.

Generation of dynamic light fields. A digital micromirror device (DMD) module (V-7000, ViaLUX) is addressed by custom software to dynamically modulate the intensity of a 532 nm laser beam (Verdi G10, Coherent). The beam is expanded upstream of the DMD, to fully cover the DMD surface. The modulated beam is then projected through a 4× microscope objective (Nikon) onto the working area containing the microrobots. The light power onto the microrobots is of the order of a few hundred milliwatts. A CMOS camera (resolution 1,280 × 1,024—Thorlabs) images the workspace through the same objective. Details of the set-up are reported in Supplementary Information 2.

Finite-element models. The numerical simulations are performed in COMSOL Multiphysics (COMSOL). For the cylinders a two-dimensional (2D)-axisymmetric stationary analysis is performed, whereas a 3D stationary analysis is done for the discs. The models simulate the solid mechanics of the microstructures and do not take into account the absorption of light, the conduction of heat through the material, or the hydrodynamic response of the surroundings. Strains arise in proportion to a locally imposed reduction of the order parameter Q. For additional details refer to Supplementary Information 5.

Deformation experiments. For the top-view experiments, an LCE cylinder is positioned on a glass covered with polytetrafluoroethylene (PTFE) tape. The sample is excited with a linear periodic binary light pattern (rectangular wave: frequency $f = 1$ Hz, effective pattern wavelength $\lambda = 950\,\mu$m, and duty cycle $dc = 1/3$; see Supplementary Information 6).

For the side-view experiments, an LCE cylinder is positioned on a glass covered with a thin layer of silicone oil to avoid adhesion. An additional camera (Dragonfly 2 HIBW, Point Grey Research) is placed to the side of the workspace where it images the cylinder through a 10× microscope objective (Nikon). A linear periodic binary light pattern (rectangular wave: $f = 1$ Hz, $\lambda = 260\,\mu$m, $dc = 1/3$) is projected onto the sample.

Swimming experiments. In the first swimming experiment, a cylindrical LCE sample is suspended far from any solid surface in a solution of glycerol and water, in which a density gradient is established. A linear periodic binary light pattern (rectangular wave: $f = 2$ Hz, $\lambda = 390\,\mu$m, $dc = 1/3$) is projected onto the sample. First, the light pattern travels from left to right for about 50 s, then the LCE is allowed to relax for about 10 s, and then a light pattern travelling from right to left is projected for another 50 s.

In the wavelength-dependence analysis, linear periodic binary light patterns with varying wavelengths ($f = 3$ Hz, $dc = 0.3$) are projected onto the sample for 10 s each. After each projection, the sample is allowed to relax for 5 s. The swimming speeds are evaluated from the displacements estimated by automatic thresholding and particle analysis (ImageJ).

2D-locomotion and rotation experiments. A disc is immersed in silicone oil close to the bottom of a Petri dish covered with a thin layer of polydimethylsiloxane (PDMS). For the 2D-locomotion tests, a closed-loop control algorithm tracks the microrobot's position and projects a bounded linear periodic light pattern onto it (square wave: $f = 3$ Hz, $\lambda = 650\,\mu$m). The travelling direction of the wave pattern is automatically calculated to drive the disc towards the next target position in the route. The rotations are driven by azimuthal square waves ($f = 3$ Hz, $\lambda = 2\pi/3$ rad, see Supplementary Information 6) centred on the disc. The light pattern is rotated clockwise for 60 s, and then anticlockwise for another 60 s. The rotation of the disc is estimated by measuring the position of a small defect on its edge, used as fiducial mark, with respect to its centre.

Multiple microrobots experiments. The two small discs are immersed in silicone oil, close to the bottom of the PDMS-coated Petri dish, and close enough to each other to fit within the workspace. Independent periodic binary light patterns are projected onto the two discs (azimuthal square waves: $f = 3$ Hz, $\lambda = \pi$ rad). In the first 60 s, both light patterns are rotated in an anticlockwise direction; for the next 60 s, the pattern on the left disc is reversed.

Code availability. The custom code for DMD control is available on request by contacting the corresponding author.

nature materials
SUPPLEMENTARY INFORMATION
DOI: 10.1038/NMAT4569

Structured light enables biomimetic swimming and versatile locomotion of photoresponsive soft microrobots

Stefano Palagi[1], Andrew G. Mark[1], Shang Yik Reigh[2], Kai Melde[1], Tian Qiu[1,3], Hao Zeng[4], Camilla Parmeggiani[4,5], Daniele Martella[4], Alberto Sanchez-Castillo[1], Nadia Kapernaum[6], Frank Giesselmann[6], Diederik S. Wiersma[4], Eric Lauga[2] and Peer Fischer[1,6]*

[1] Max Planck Institute for Intelligent Systems, 70569 Stuttgart, Germany

[2] Department of Applied Mathematics and Theoretical Physics, Centre for Mathematical Sciences, University of Cambridge, Cambridge, CB3 0WA, United Kingdom

[3] Institute of Bioengineering, Ecole Polytechnique Fédérale de Lausanne (EPFL), CH-1015 Lausanne, Switzerland

[4] European Laboratory for Non Linear Spectroscopy (LENS), University of Florence, 50019 Sesto Fiorentino, Italy

[5] CNR-INO, 50019 Sesto Fiorentino, Italy

[6] Institut für Physikalische Chemie, Universität Stuttgart, 70569 Stuttgart, Germany

Contents

S1. Supplementary Movies Description

1) Travelling-wave deformation of cylindrical LCE microrobots.

   Top view. The LCE cylinder (length of about 1.3 mm and radius of about 170 μm) is positioned on a glass slide covered with PTFE tape and excited with a linear periodic binary light pattern (frequency f = 1 Hz, wavelength λ = 950 μm and duty cycle dc = 1/3).

   Side view. The LCE cylinder (radius of about 100 μm) is positioned on a glass slide covered with a thin layer of silicone oil to avoid adhesion and excited with a linear periodic binary light pattern (frequency f = 1 Hz, wavelength λ = 260 μm and duty cycle dc = 1/3).

2) Forward and reverse swimming of a cylindrical LCE microrobot (speed: 2X).

   The cylindrical LCE sample (length of about 1.2 mm, radius of about 120 μm) is suspended in a solution of glycerol and water, in which a density gradient is established. A linear periodic binary light pattern (frequency f = 2 Hz, λ = 390 μm and duty cycle dc = 1/3) is projected onto the sample. First the light pattern travels from left to right, then it is turned off to let the LCE relax for about 10 s, and then turned back on with a travelling direction from right to left.

3) Versatile locomotion of LCE disk-shaped microrobots (diameter of 400 μm). The disk is immersed in silicone oil and allowed to settle close to the bottom surface, which is covered with polydimethylsiloxane (PDMS).

   Square path (closed loop control with automatic tracking; speed: 4X). Linear periodic light patterns (square waves with frequency f = 3 Hz and wavelength λ = 650 μm) with proper travelling direction are projected onto the disk to drive it towards the next target position in the route.

   Diamond-shaped path (closed loop control with automatic tracking; speed: 4X). Linear periodic light patterns (square waves with frequency f = 3 Hz and wavelength λ = 650 μm) with proper travelling direction are projected onto the disk to drive it towards the next target position in the route.

In-place rotation (closed loop control with automatic tracking; speed: 10X). Azimuthal periodic light patterns (square waves with frequency f = 3 Hz and wavelength $\lambda = 2\pi/3$ rad) rotating first clockwise and then counter-clockwise are projected onto the disk.

4) Independent control of two disks (diameter of 200 μm). The disks are immersed in silicone oil and allowed to settle close to the bottom surface, which is covered with polydimethylsiloxane (PDMS).

Independent in-place rotation (closed loop control with automatic tracking; speed: 10X). Azimuthal periodic light patterns (square waves with frequency f = 2 Hz and wavelength $\lambda = \pi/2$ rad) rotating first both clockwise and then one (right) clockwise and one (left) counter-clockwise are projected onto the disks.

Independent horizontal translation (closed loop control with automatic tracking; speed: 10X). Linear periodic light patterns (square waves with frequency f = 3 Hz and wavelength λ = 200 μm) are projected onto the disks to drive them in opposite directions. As they approach, the disks experience an attractive hydrodynamic interaction.

S2. Description of the optical setup

The system for generating dynamic light fields is represented in Fig. S1. The laser beam is first expanded (expansion factor changed according to needs: typically, a 5X expansion was used for deformation and swimming experiments, 8X for disks' locomotion experiments) and then directed on the Digital Micromirror Device (DMD; Vialux V-7000). We use an angle of incidence of 32°, rather than the conventional 24° to achieve optimal blazing for coherent 532nm light. The pattern generated on the DMD by the control software is imaged by the tube lens L3 (focal length: 300 mm) and the light field is projected onto the microrobots by means of a 4X microscope objective. The workspace is imaged through the same objective and the lens L4 (focal length: 200 mm) by a CMOS camera. To collect the light to the camera, a beam splitter is inserted in the main optical path. An additional short pass filter is added in front of the camera to filter out any residual reflection of the laser beam. Typical laser illumination powers, with all DMD pixels in the on state, are up to 2.5 W distributed over the entire workspace and depend on experimental conditions (mainly beam expansion, fluid surrounding the microrobots).

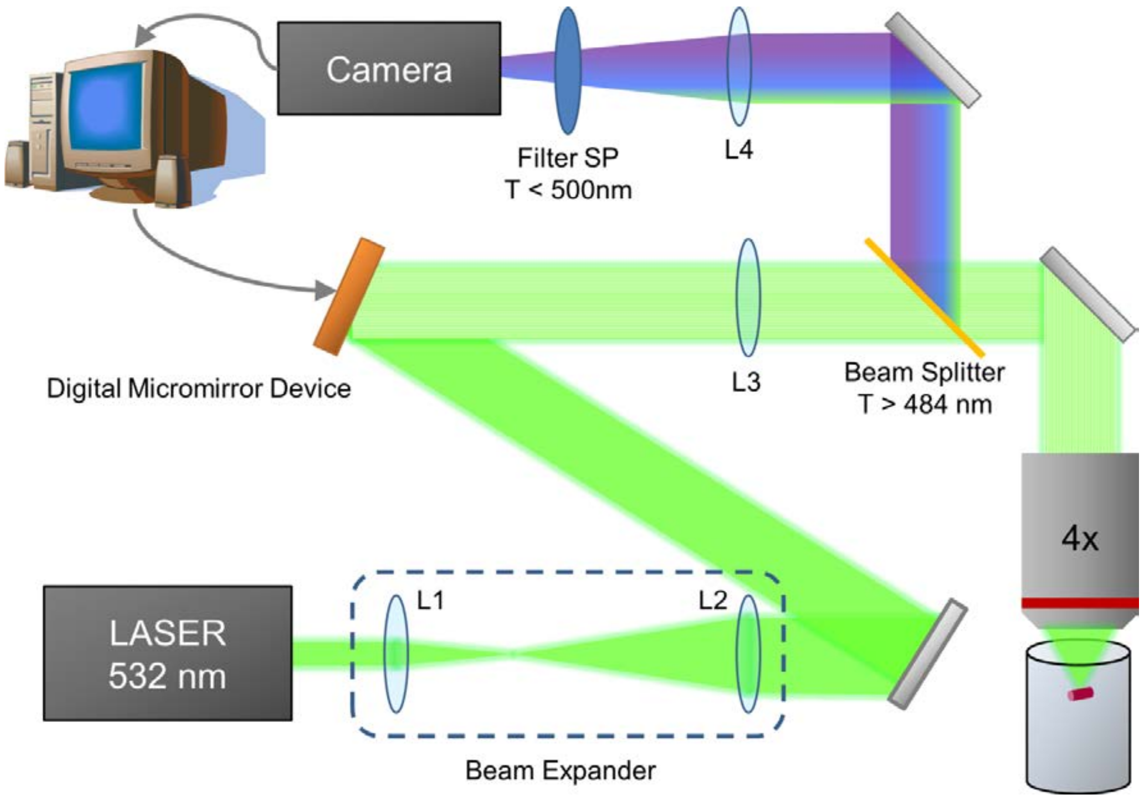

Figure S1. Schematic of the optical setup for the generation of dynamic light fields

S3. Chemicals compounds composing the LCEs

Preparation of LCEs by photopolymerization of acrylate moieties requires monomeric mixtures that contain, at least, a mesogenic monomer (**M1** or **M2**), responsible for the alignment inside the material, and a cross-linker (**CL1** or **CL2**) which determines the mechanical properties of the polymer. A photo-initiator is also required to synthesize the polymeric network in one step allowing the simultaneous grown of the polymeric chains and their crosslinking. Moreover, adding an azo-dye in such mixtures leads to a photosensitive material. Monomers **M1** and **M2** and azo dye were prepared by some of us as previously reported[1,2]. The cross-linker **CL1** and the photo-initiator are used as purchased from Sigma-Aldrich, Germany. The cross-linker **CL2** is used as purchased from Synthon Chemicals, Germany.

The azo-dye embedded within the LCEs has a strong absorption in the visible and a push-pull electronic structure, because of which we expect the thermal reconversion from the *cis* to the *trans* state to be in the millisecond range[3]. This timescale is further decreased as the azo-dye is chemically bonded to the polymer backbone[4]. Under light excitation, the crosslinked dye molecules inside the LCE network absorb photons and undergo *trans* to *cis* isomerization acting as a non-mesogenic impurity. However, due to the low dye concentration and to the fast thermal relaxation, which transfers energy into the network, we assume the LCEs' phase transition to be mostly achieved by a light-induced thermal effect.

Monomers

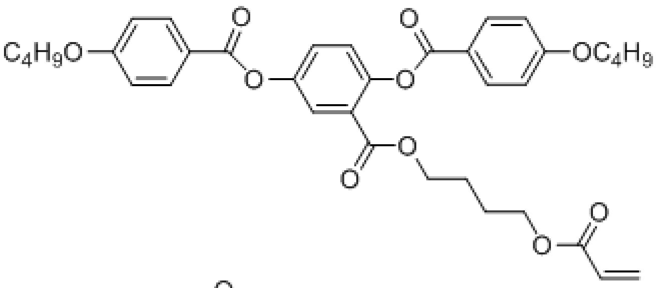

M1

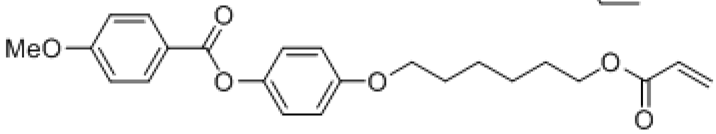

M2

Crosslinkers

CL1 1,6-Hexanediol diacrylate

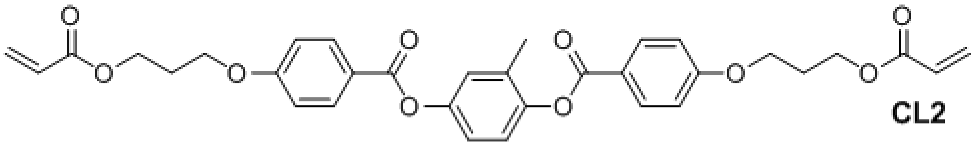

CL2

1,4-Bis-[4-(3-acryloyloxypropyloxy)benzoyloxy]-2-methylbenzene

Azo-dye

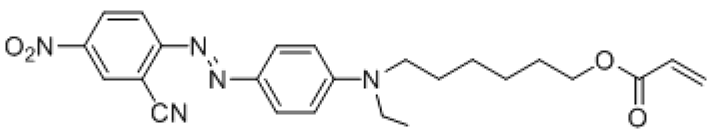

Photoinitiator

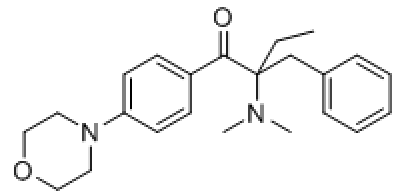

2-Benzyl-2-(dimethylamino)-4'-morpholinobutyrophenone

S4. Small Angle X-ray Scattering

Small angle X-ray scattering measurements are conducted on a Bruker AXS NanoStar diffractometer using Cu Kα radiation at 1.54 Å. A cylindrical fibre is clamped in a temperature controlled sample holder leaving a roughly 2 mm length unconstrained and free-hanging. The temperature is ramped through the nematic to isotropic transition from 70°C to 120°C over approximately 7 hrs. At each temperature, two measurements are made. First, an X-ray nanography image is acquired giving a detailed measurement of the longitudinal contraction; second, a 2D diffractogram with 30 min integration time is collected to identify the mesogen alignment (Fig. S2). A background subtraction to correct for inelastic scattering was performed on the diffraction patterns before further analysis. The orientational order is quantified by first fitting the azimuthal intensity profile (Fig. S3) with the expression[5,6]

$$I(\chi) = \sum_{n=0}^{N} f_{2n} \frac{2^n n!}{(2n+1)!!} \cos^{2n} \chi \,, \tag{S1}$$

where χ is the azimuthal angle, and f_{2n} are the expansion coefficients. Limiting the summation to $N = 4$ is sufficient for convergence. The orientational order parameter is calculated from the expansion coefficients according to

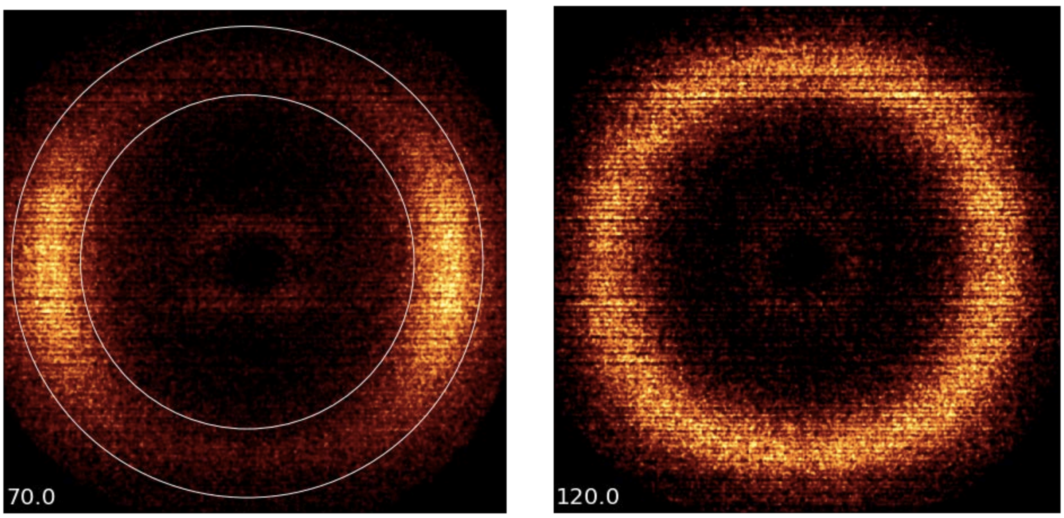

Figure S2. SAXS Diffraction Patterns Cylindrical fibre samples in the nematic (70°C, left) and isotropic phases (120°C, right). The fibre axis is oriented vertically.

$$Q = \langle P_2 \rangle = \frac{\sum_{n=0}^{N} f_{2n} \frac{2n}{4(n+1)^2 - 1}}{\sum_{n=0}^{N} f_{2n} \frac{f_{2n}}{2n+1}}. \quad \text{(S2)}$$

At 70°C, this gives $< P_2 > = 0.376 \pm 0.007$ and at 120°C $< P_2 > = 0.000 \pm 0.004$. The temperature dependent results (Fig. S4) show a close correlation between the longitudinal deformation (red) and the degree of orientational order (blue) through the phase transition.

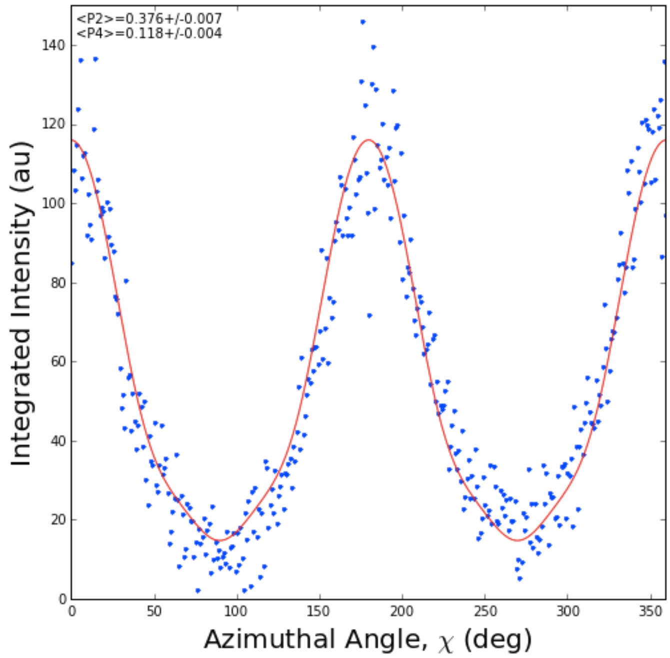

Figure S3. Radially integrated SAXS diffraction intensity for 70°C. The red line is a fit to the data based on equation (S1) with $N = 4$. The radial limits to integration are indicated by the annulus in Fig. S2 (left).

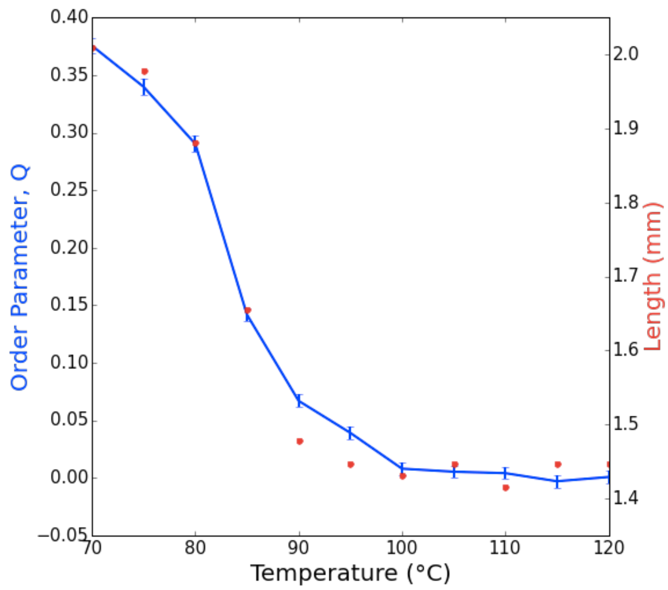

Figure S4. Correlation between the orientational order parameter and fibre deformation.

S5. Modelling the LCEs' deformation

The deformation of LCEs is associated with changes in the nematic order and can thus be expressed as a function of the order parameter Q. This synthetically describes the orientation of the liquid crystalline molecules with respect to the nematic director and assumes values ranging between 0 (disorder, random orientation) and 1 (perfect order, all molecules perfectly aligned along the director). Across the transition from the nematic, ordered phase ($Q = Q_N$) to the isotropic, disordered phase ($Q \approx 0$), the material undergoes a contraction Λ along the nematic director such that

$$\Lambda = \frac{L}{L_N} = \left(\frac{1\ +\ 2Q_N}{1 - Q_N}\right)^{-\frac{1}{3}} \tag{S3}$$

where L and L_N represent the length of the elastomer along the nematic director in the deformed and relaxed (nematic) configurations, respectively[7]. Simultaneously, the elastomer experiences an expansion corresponding to $\Lambda^{-1/2}$ in the two orthogonal directions, so that the volume is constant through the transition. The deformation tensor $\boldsymbol{\Lambda}$ can thus be expressed as

$$\boldsymbol{\Lambda} = \begin{bmatrix} \Lambda^{-\frac{1}{2}} & 0 & 0 \\ 0 & \Lambda^{-\frac{1}{2}} & 0 \\ 0 & 0 & \Lambda \end{bmatrix} \tag{S4}$$

where the reference frame is defined such that the z-axis corresponds to the nematic director $\boldsymbol{n}$. From this we can derive, in the same reference frame, a strain tensor ε as follows

$$\varepsilon = \begin{bmatrix} \frac{1-\Lambda}{2\Lambda} & 0 & 0 \\ 0 & \frac{1-\Lambda}{2\Lambda} & 0 \\ 0 & 0 & \frac{1}{2}(\Lambda^2 - 1) \end{bmatrix} \tag{S5}$$

The numerical simulations were performed in COMSOL Multiphysics using the Solid Mechanics module. The LCEs are modelled as nearly incompressible (Poisson's ratio $\nu \approx 0.5$) linear elastic materials. A scalar field Q describes the spatial distribution of the liquid crystalline order parameter. In particular, the local value of Q was assumed to be directly related to the imposed light distribution, such that $Q = Q_N$ where the light is off and $Q = 0$ where the light is on (see Fig. S5). The corresponding strain distribution is then applied to the material according to the strain tensor defined in equation (S5). In this way, the macroscopic shape change of the material is simulated starting from a pre-defined light distribution, mediated by the order parameter.

For the cylindrical microrobots, we set $Q_N = 0.376$, according to the experimental results from X-ray scattering, and we assumed an elastic modulus of 1 MPa. For the disks, we assumed $Q_N = 0.25$ (corresponding to the reported 20% maximum strain) and we set the elastic modulus to 1.3 MPa as reported in Ref [8].

S6. Definition of the features of the projected patterns

The projected light patterns are defined starting from a rectangular wave function of this kind:

$$\mathrm{rect}(w) = \begin{cases} 1 & \left|w - \frac{1}{2}\right| \leq \frac{dc}{2} \\ 0 & \left|w - \frac{1}{2}\right| > \frac{dc}{2} \end{cases} \tag{S6}$$

where dc is the duty cycle (ratio between on-time and period, see Fig. S5) and

$$w = \mathrm{mod}\left(\frac{x}{\lambda} - ft\right). \tag{S7}$$

The variables x and λ represent the spatial coordinate and the wavelength, respectively (both can be either linear or angular – see Fig. S6).

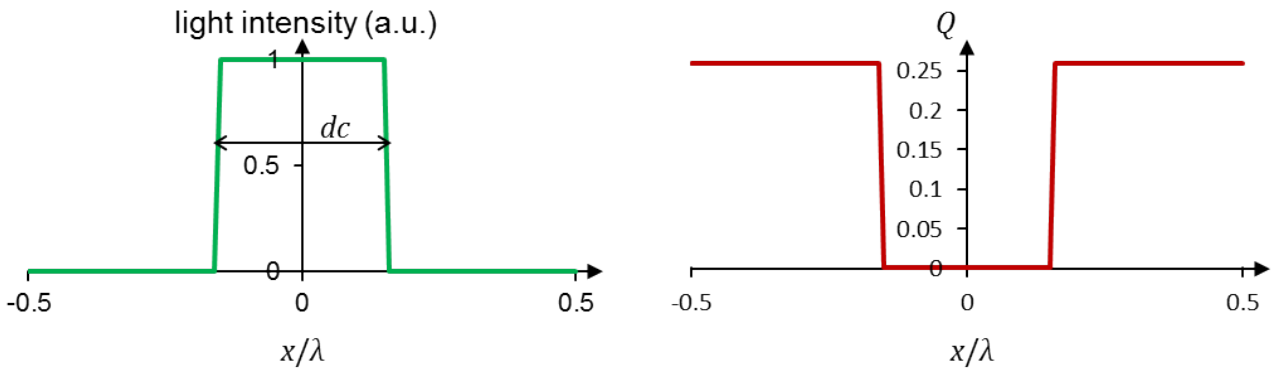

Figure S5. Typical binary light distribution (left) and corresponding theoretical value of the order parameter Q (right).

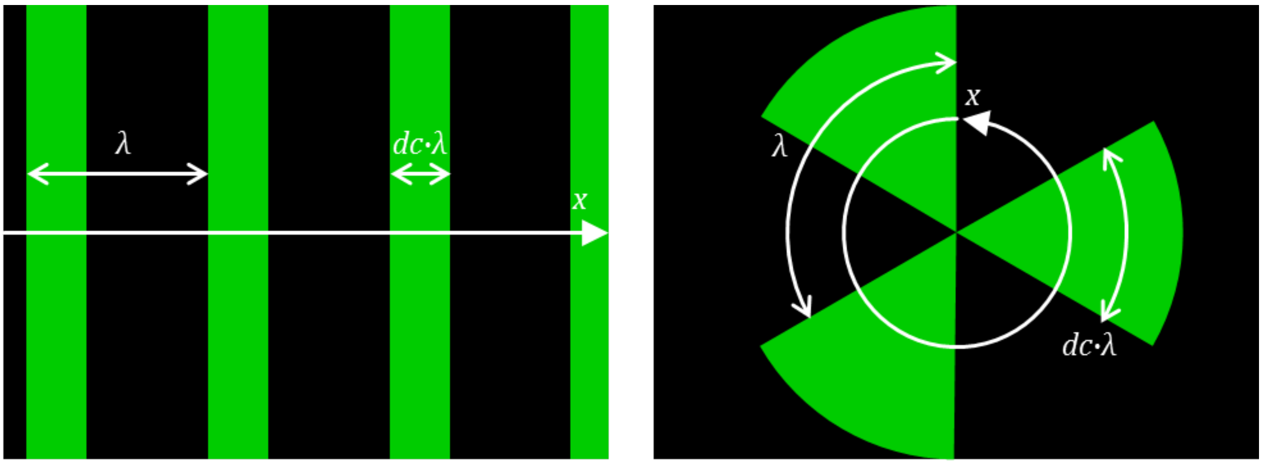

Figure S6. A linear (left) and an azimuthal (right) binary patterns.

S7. Dependence of deformation amplitude on wavelength

The expression and parameters presented in equation (3) in the main text were derived from side-view videos acquired from anchored cylinders of liquid crystal elastomer (Supplementary Movie 1). We have experimentally observed that when a binary light pattern (rectangular wave) is applied, the material deforms in a similar fashion, but rather than exactly matching the abrupt, discontinuous transition between light and dark regions the deformation profile is smoother. This arises from the material's continuity conditions and finite Young's modulus: the radial expansion of illuminated regions is restricted in the vicinity of undeformed dark areas. Because of this smoothing effect, when the wavelength of the illumination profile decreases, the peaks of the deformation profiles get closer, superpose and cancel out (because of volume conservation). Therefore, the amplitude of the wave deformation shows a dependence on the wavelength, which we describe by the empirical equation (3).

We have developed an analytical model to represent deformation profiles like the one extracted from the frame in Fig. S7. We have assumed that each discontinuity in the binary intensity profile results in a continuous sigmoidal transition in the actual material deformation. In particular,

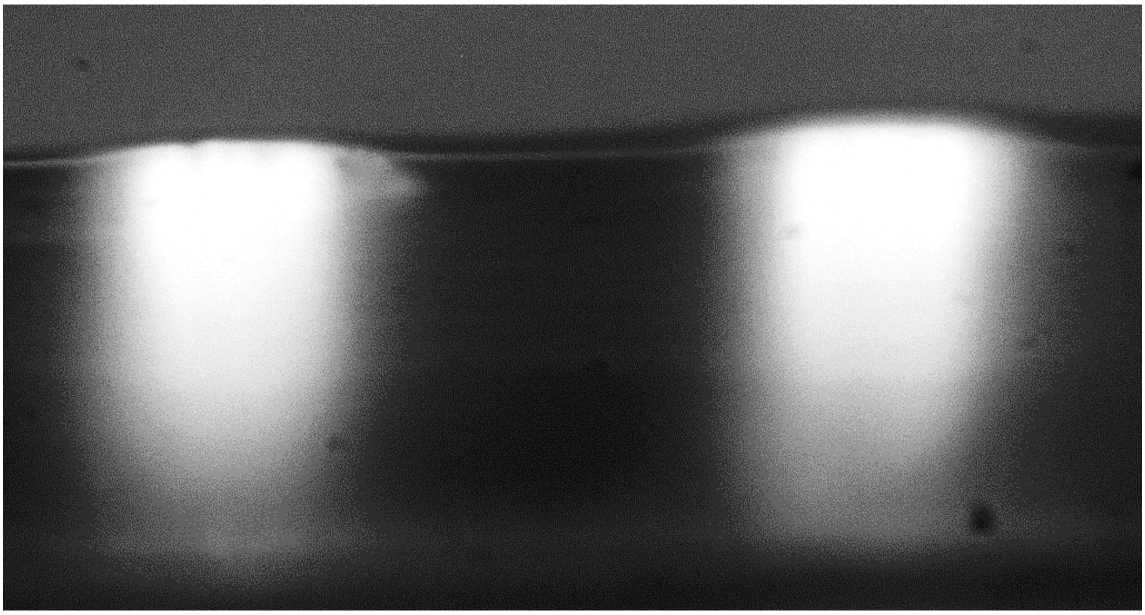

Figure S7. Deformation of a cylindrical sample of LCE under a binary light pattern imaged from the side. Frame from a video showing the deformation of a cylinder of LCE under a binary light pattern (rectangular wave, dc = 0.3) travelling from left to right. The cylinder is 100 μm in radius.

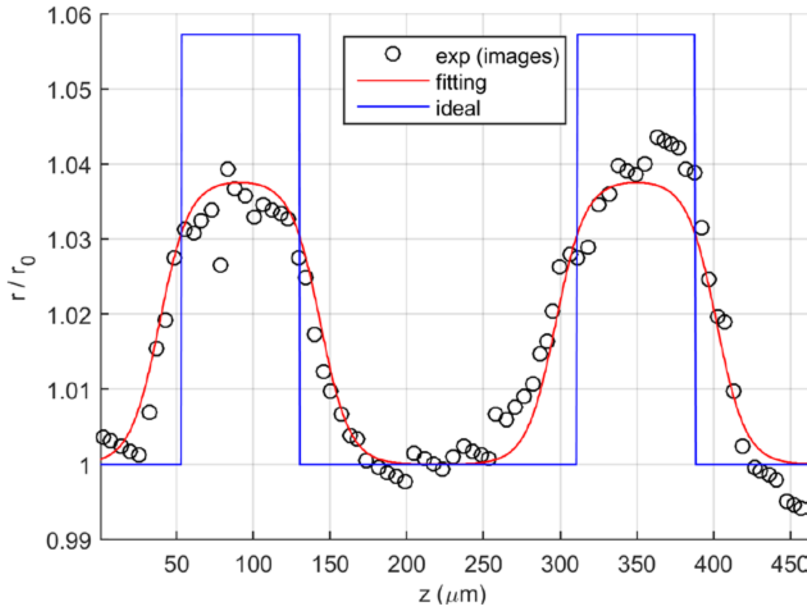

Figure S8. Fitting of the smoothing function on the experimental profile. Data on the deformation profile, along with the fitting result and the ideal rectangular profile. Experimental data taken from the 100 μm radius fibre shown in Fig. S7 with binary light pattern $f = 1$ Hz, $\lambda = 260$ μm, $dc = 1/3$

referring to the rectangular wave defined above, the function describing the deformation is assumed to be of the following form

$$prof(w) = \left(1 + \mathrm{e}^{-\frac{\lambda}{\gamma}\left(w - \frac{1+dc}{2}\right)}\right)^{-1} - \left(1 + \mathrm{e}^{-\frac{\lambda}{\gamma}\left(w - \frac{1-dc}{2}\right)}\right)^{-1}, \tag{S8}$$

where γ is the smoothing parameter. By fitting this smoothing function to the experimental profile, we obtain the smoothing parameter γ, which describes the steepness of the transitions (Fig. S8). We further assume that γ is characteristic of the material and sample under consideration, and that it is independent of the wavelength of the applied profile. Then we simulate what happens at other wavelengths while keeping γ fixed (Fig. S9).

Finally, we have extracted the amplitude of radial expansion at different wavelength (Fig. S10), which can be expressed as

$$b_r = b_r^0\left(1 - e^{-\frac{\lambda}{\lambda_C}}\right). \tag{S9}$$

where we have introduced the empirical constant λ_C, which characterizes the cutoff wavelength below which the deformation amplitude becomes attenuated. Smaller λ_C implies a lower smoothing effect and a better spatial resolution of the material. The value of λ_C that we have estimated according to this analysis for this specific cylindrical microrobot is about 80 μm.

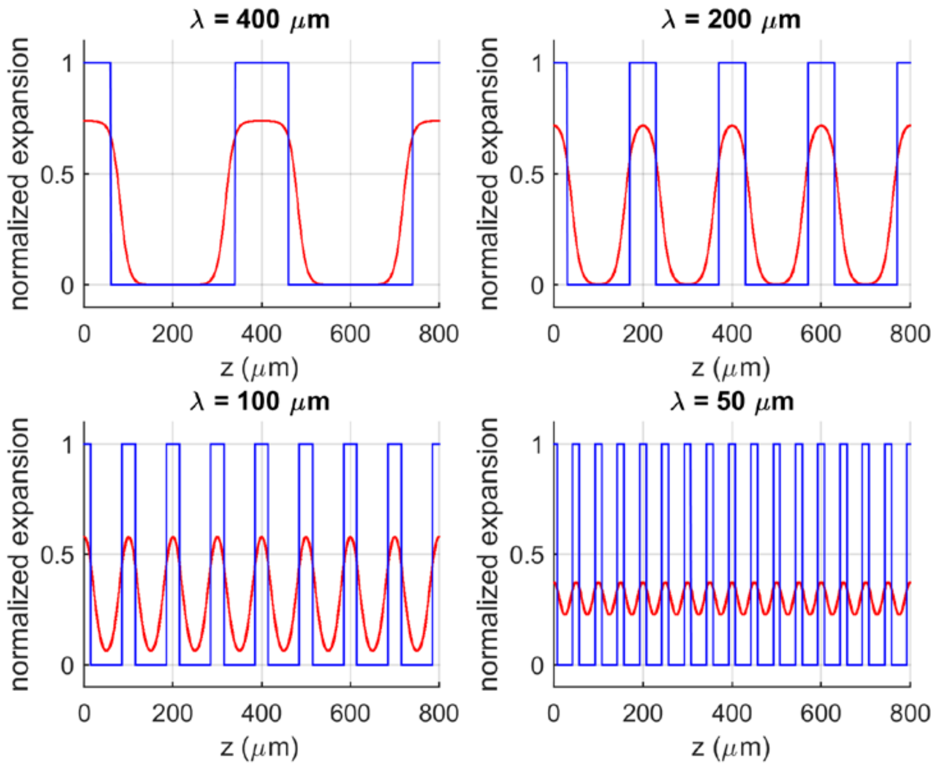

Figure S9. Smoothing at different wavelengths. The imposed illumination profile (blue) compared with the resulting material deformation (red) calculated using Eqn. S8. The graphs show how the deformation profile, and especially its amplitude, changes at various wavelengths. Model parameters were derived from the experimental fit in Fig. S8.

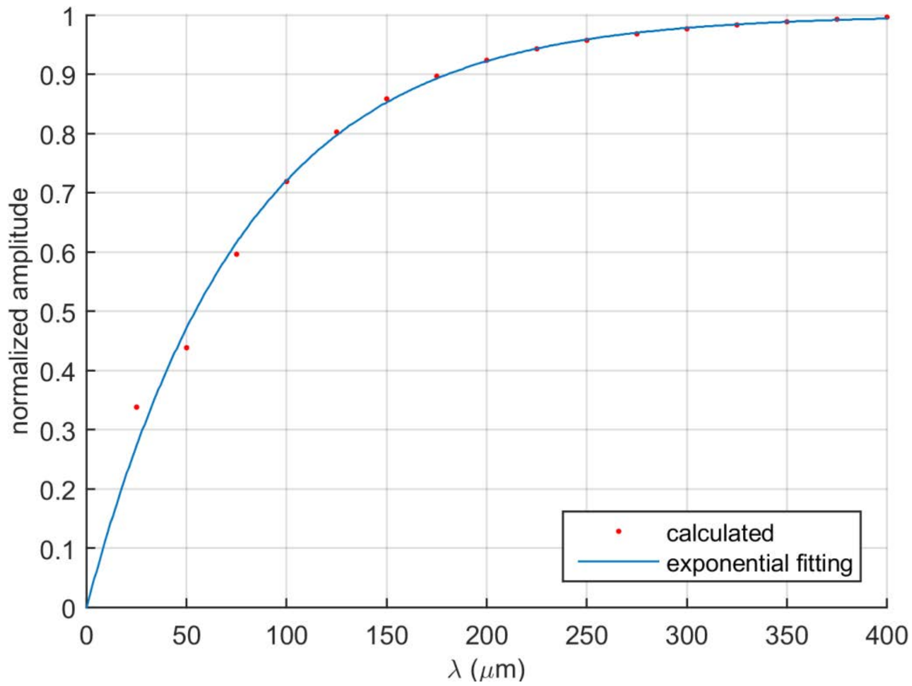

Figure S10. Simulated deformation amplitude (*b*) as a function of illumination wavelength. The red points were derived from simulated deformation profiles like those in Fig. S9 using model parameters derived from the experimental fit in Fig. S8. The blue line is a fit in the form of Eqn. S9 yielding a critical wavelength of 80 μm.

S8. Finite element model analysis of the dependence of deformation amplitude on wavelength

To further illuminate this behaviour, we have also investigated it using the finite element model previously described. The deformation profiles of a 100 μm radius cylinder were simulated for a range of illumination wavelengths. The structure was modelled using the same parameters described in S5: Young's modulus 1 MPa, Poisson's Ratio 0.5, order parameter $Q_N = 0.376$.

Figure S11 shows the deformation profile in terms of the wavelength reduced longitudinal coordinate in response to a square-wave illumination profile. Consistent with the empirical model in Section S7, the deformation amplitude dramatically decreases (Fig S12, green curve) with wavelength below the critical wavelength.

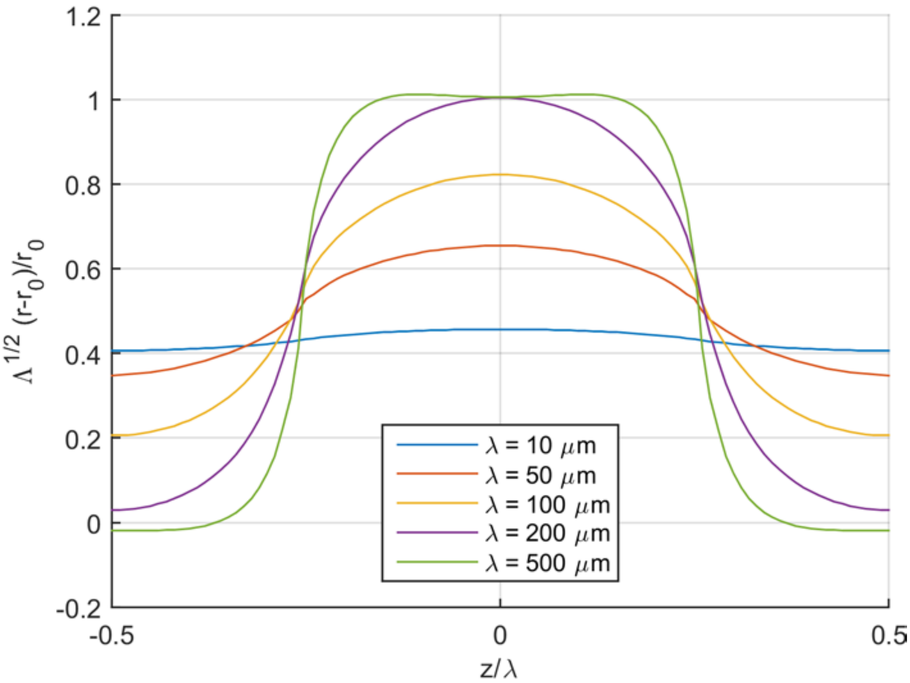

Figure S11. Numerically calculated normalized deformation profiles for different wavelengths of a square wave illumination profile. At short wavelengths the deformation profile is almost flat (small wave amplitude). The radius of the simulated cylinder is 100 μm.

We have also addressed how the size of the cylinder affects the critical wavelength. The results, shown in Fig. S12, indicate that λ_C depends linearly with the cylinder radius ($\lambda_C = 1.15\ r$). This means that small cylinders can resolve narrower spatial features, so that deformation profiles with shorter wavelengths can in principle be obtained. This is important in view of down-scaling of the swimming microrobots (shorter wavelengths correspond to higher swimming speed).

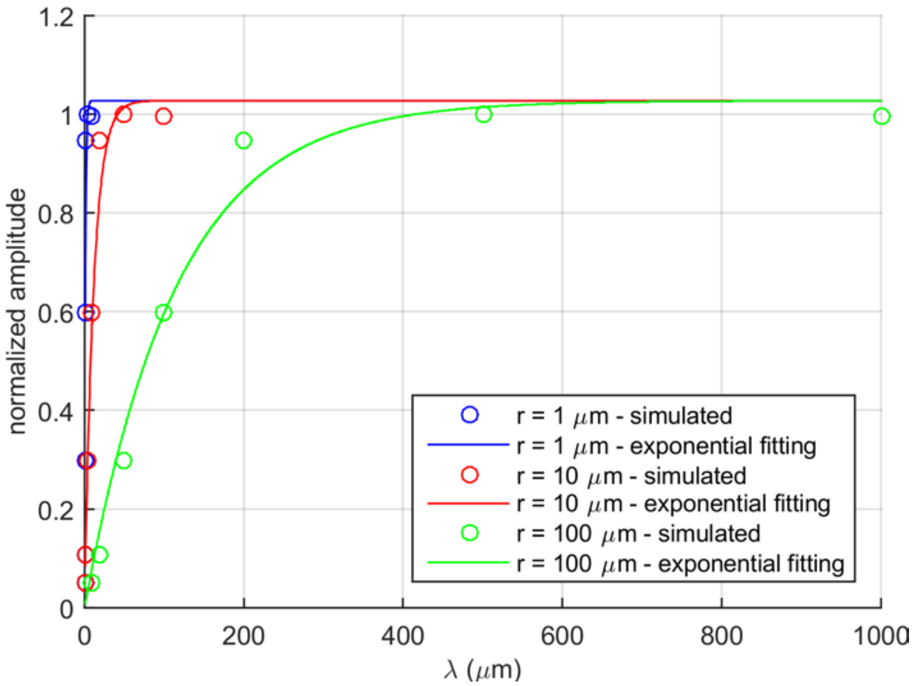

Figure S12. Normalized wave amplitude dependence on the wavelength from numerical simulations for different radii of the cylinder. Small cylinders have smaller λ_c and can therefore resolve narrower spatial features. Fits are based on Eqn. S9.

S9. Derivation of analytical model for cylinder swimming

We now detail the mathematical model for the propulsion of the cylindrical elastomer, with notation shown in Fig. S13. The wave on the cylindrical surface is assumed to undergo both axial and transverse deformations. In the frame of reference moving with propulsion velocity V, the axisymmetric wave may be described in cylindrical coordinate (r,φ,z) as the material positions (r_S,z_S) on the surface of the cylinder given by

$$\begin{aligned} r_S &= a + b\sin k(z+Ut) \\ z_S &= z + d\cos k(z+Ut) \end{aligned} \tag{S10}$$

where t is time, a the equilibrium radius of the cylinder, b the amplitude of the deformation in the radial ($\boldsymbol{e}_r$) direction, d the amplitude of the deformation in the axial ($\boldsymbol{e}_z$) direction, z the Lagrangian rest position of the cylinder (*i.e.* before deformation), k the wave number ($k = 2\pi/\lambda$ where λ is the wavelength), and $U = \lambda f$ the velocity of the wave in the moving frame.

Assuming the cylinder to be incompressible, the value of d may be evaluated in terms of that of b. Consider a cylindrical section with of small thickness dz in an undeformed body

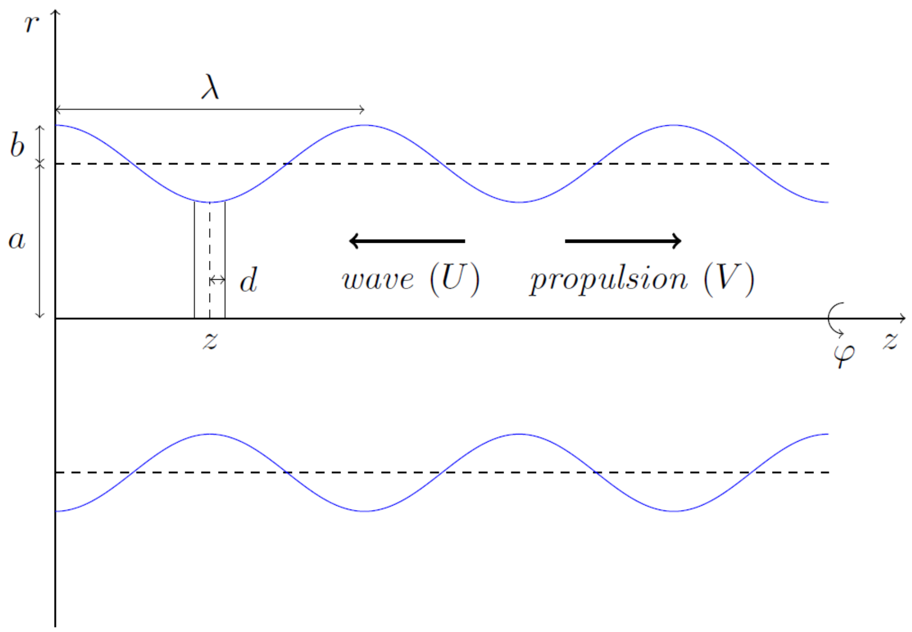

Figure S13. Model for light-induced deformation of elastomer. Infinite cylinder undergoing axial and transverse deformations in the cylindrical coordinate system (r,φ,z). The radius of the cylinder is a, b is the amplitude of the transverse deformation, d is the amplitude of the axial deformation, and λ is the wavelength. The wave travels at velocity U in the frame of the moving cylinder, which is propelled at velocity V in the laboratory frame.

which is extended in the r direction and contracted in the z direction. Given the sinusoidal deformation assumed in equation (S10), the deformed volume of the cylindrical section is approximately given by

$$\pi r_s^2 dz_s \approx \pi a^2 dz \left\{1 + \frac{2b}{a} \sin k(z + Ut) - d\, k \sin k(z + Ut)\right\} \tag{S11}$$

and the volume remains constant and first order in the amplitude provided that $d = \alpha b$ with $\alpha = 2/(ka)$.

The propulsion velocity of the cylinder and the fluid velocity at low Reynolds number are determined by solving the incompressible Stokes equations *i.e.*

$$\nabla p = \mu \nabla^2 \boldsymbol{v}, \qquad \nabla \cdot \boldsymbol{v} = 0 \tag{S12}$$

where p is the dynamic pressure, μ the dynamic viscosity, and $\boldsymbol{v}$ the fluid velocity. In cylindrical coordinates, the fluid velocity field $\boldsymbol{v} = (v_r, v_\varphi, v_z)$ is axisymmetric and its velocity components satisfy

$$\begin{aligned} \frac{1}{\mu}\frac{\partial p}{\partial r} &= \nabla^2 v_r - \frac{v_r}{r^2}, \\ \frac{1}{\mu}\frac{\partial p}{\partial z} &= \nabla^2 v_z, \\ \frac{\partial v_r}{\partial r} + \frac{v_r}{r} + \frac{\partial v_z}{\partial z} &= 0. \end{aligned} \tag{S13}$$

Using the notation $y \equiv kr$ and $s \equiv k(z + Ut)$, the solutions to equation (S13) are given by linear combinations of following general solutions for various integer numbers n

$$\begin{aligned} p &= \mu k p_n \cos(ns), \\ v_r &= u_n \cos(ns), \\ v_z &= w_n \sin(ns), \end{aligned} \tag{S14}$$

where

$$\begin{aligned} p_n &= 2A_n n K_0(ny), \\ u_n &= A_n n y K_0(ny) + B_n K_1(ny), \\ w_n &= (B_n - 2A_n) K_0(ny) + A_n n y K_1(ny), \end{aligned} \tag{S15}$$

with K_i denoting the modified Bessel function of the second kind ($i = 0,1$), and with the unknown constants A_n and B_n to be determined by the boundary conditions[9].

In the frame moving with the cylinder at velocity V, the boundary conditions on the surface of the elastomer are given from equation (S10) by

$$\begin{aligned} v_r(r_s, z_s) &= Ubk\cos k(z+Ut), \\ v_z(r_s, z_s) &= -Udk\sin k(z+Ut). \end{aligned} \qquad \text{(S16)}$$

Assuming that the transverse deformation of the cylinder is small, we may obtain the leading-order approximate solution for the velocity field by evaluating u_1 and w_1 at $r = a$ in equation (S16). Then, the unknown constants A_1 and B_1 are easily found as

$$\begin{aligned} A_1 &= \frac{Ubk}{\phi(y_1)}\{K_0(y_1) + \alpha K_1(y_1)\}, \\ B_1 &= \frac{Ubk}{\phi(y_1)}\{(2-\alpha y_1)K_0(y_1) - y_1 K_1(y_1)\}, \end{aligned} \qquad \text{(S17)}$$

where $\phi(y) = yK_0^2(y) - yK_1^2(y) + 2K_0(y)K_1(y)$ and $y_1 \equiv ka$.

Since this solution at first order in bk does not contribute the propulsion of the cylinder[9,10], we next consider the solutions at order $(bk)^2$ using a Taylor expansion as

$$v_\nu^{(2)}(r_s, z_s) = v_\nu^{(1)}(a, z) + \left.\frac{\partial v_\nu^{(1)}}{\partial r}\right|_{a,z}(r_s - a) + \left.\frac{\partial v_\nu^{(1)}}{\partial z}\right|_{a,z}(z_s - z)\,, \qquad \text{(S18)}$$

where ν denotes r or z, $v_\nu^{(1)}$ is the solution at first order (i.e. $v_r^{(1)} = u_1(y)\cos(s)$ and $v_z^{(1)} = w_1(y)\sin(s)$), and $v_\nu^{(2)}$ the solution at second order. The boundary conditions, equation (S16), for the velocity of the fluid at the surface of the cylinder may be satisfied by choosing the solution at order two among the general solutions from equation (S15) and equation (S18) at $r = a$.

In the moving frame of reference with the propulsion velocity V, the conditions are written by

$$\begin{aligned} Ubk\cos(s) &= \left[u_1\cos(s) + \frac{1}{2}bk(u_1' - \alpha u_1)\sin(2s) + u_2\sin(2s)\right]_{y=y_1}, \\ -Udk\sin(s) &= \left[w_1\sin(s) + \frac{1}{2}bk\{(w_1' + \alpha w_1) - (w_1' - \alpha w_1)\cos(2s)\} + w_2\cos(2s)\right]_{y=y_1} - V, \end{aligned} \qquad \text{(S19)}$$

where the derivatives are calculated with respect to y. Equating powers of bk at order two between both sides of this equation leads to

$$V = \frac{1}{2} bk\{w_1'(y_1) + \alpha w_1(y_1)\},$$
$$u_2(y_1) = -\frac{1}{2} bk\{u_1'(y_1) - \alpha u_1(y_1)\}, \tag{S20}$$
$$w_2(y_1) = \frac{1}{2} bk\{w_1'(y_1) - \alpha w_1(y_1)\}.$$

Hence, we obtain the propulsion velocity of the cylinder as

$$V = \frac{U(bk)^2}{2}\left[\frac{(1 + 2\alpha/y_1)K_1^2(y_1) - K_0^2(y_1)}{\phi\,(y_1)/y_1} - \alpha^2\right]. \tag{S21}$$

When $y_1(\equiv ka) \to \infty$, the propulsion velocity of the cylinder reduces to the velocity of the infinite waving sheet, $V = U(bk)^2(1 + 2\alpha - \alpha^2)/2$, a classical result[11]. As one sets $\alpha = 0$, that result further reduces to the velocity of the in finite waving sheet with no axial contraction, $V = U(bk)^2/2$, the classical formula from Taylor's original work[10].

In the case where the elastomer is assumed to be incompressible, such as in the current experiments, we have to pick $\alpha = 2/(ka)$ and given that $U = \lambda f$ and $k = 2\pi/\lambda$, the propulsion velocity is given by equations (1)–(2) in the main text.

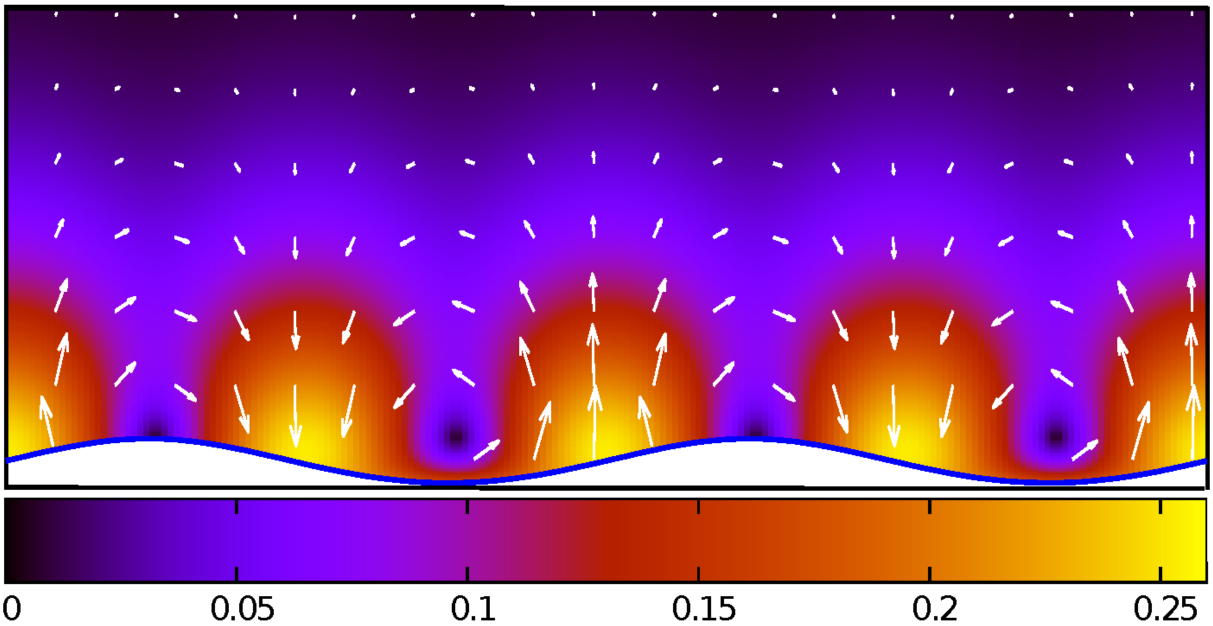

Figure S14. Predicted instantaneous fluid velocity field near the cylinder in the laboratory frame. The colour map shows the magnitudes of the fluid velocity v scaled by the wave velocity U, i.e. v/U . The white arrows indicate the direction of the fluid flow. Note the appearance of the circulating flow regions.

S10. Frequency dependence of swimming speed for cylinders

The response of one of the cylinders to wave patterns with different characteristics was also investigated. In particular, we tested rectangular wave patterns with $dc = 0.3$, to understand the dependence of the locomotion speed on frequency. The analytical model predicts that the swimming velocity is proportional to the frequency of the travelling wave deformations. However, in our experimental system the response time of the material is finite and limited by the heat transfer to the liquid. Moreover, the stress that the material can exert on the highly viscous fluid is also finite. For this reason the swimming speed may have a non-trivial dependence on the frequency of the illumination wave pattern.

All tests were performed in a glycerol-water density gradient, in the same conditions as for the experiments reported in the main text. We set the wavelength to 200 px in the camera coordinates (1 px = 1.29 μm) and we varied the frequency from 1 to 10 Hz. Each pattern was applied for 5 s, and then the cylinder was allowed to relax for 10 s in between. The net displacement for each actuation period was measured by image analysis. The results are shown in Fig. S15.

The trend reported in the graph shows that the swimming speed initially increases with frequency

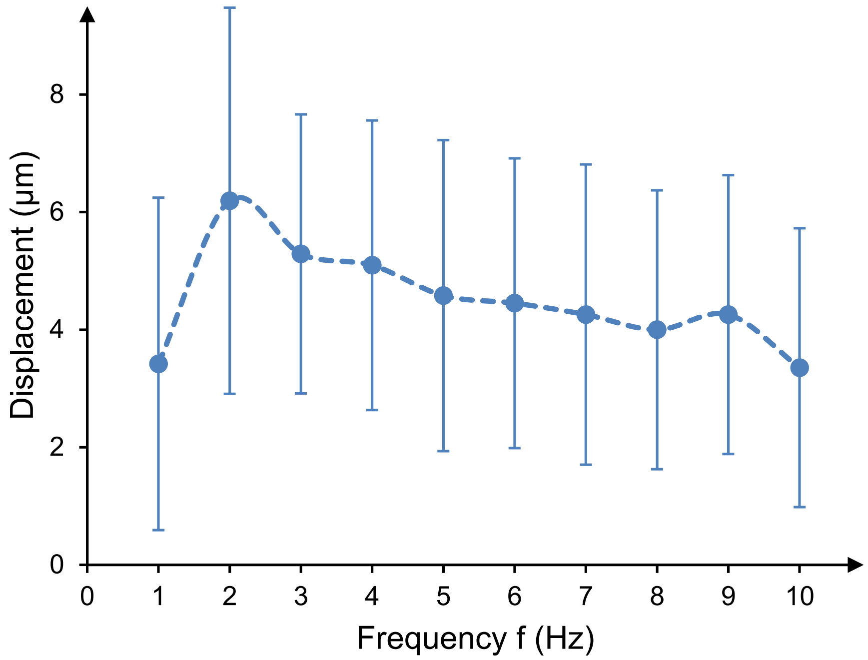

Figure S15. Frequency-dependence of the swimming of a cylinder. The wavelength was fixed to 200 px (258 μm) and the average and standard deviation reported were estimated over 2 independent tests.

up to an optimal frequency of 2 Hz. Then it starts decaying slowly as the frequency is further increased. While at low frequencies the material has enough time from one cycle to the next to fully execute its deformation stroke, at higher frequencies this is not possible and the resulting amplitude of cyclic deformation is smaller. Since the dependence of the swimming speed on the amplitude of the wave deformation is quadratic while that on the frequency is linear, the former has a larger effect, leading to the decrease in swimming speed observed in the graph.

S11. Frequency and wavelength dependence of locomotion speed for disks

The response of one of the disks to wave patterns with different characteristics was also investigated. In particular, we tested square wave patterns ($dc = 0.5$) to understand the dependence of the locomotion speed on both wavelength and frequency. All tests were performed in silicone oil, in the same conditions as for the experiments reported in the main text.

For the wavelength-dependence tests, we fixed the frequency to 2 Hz and we varied the wavelength from 100 to 800 px in the camera coordinates (1 px = 1.29 μm). For the frequency-dependence tests, we fixed instead the wavelength to 500 px in the camera coordinates and we varied the frequency from 1 to 10 Hz. Each pattern was applied for 5 s, and then the disk was let relax for 10 s in between. The net displacement for each actuation period was measured by image analysis. The results are shown in Fig. S16.

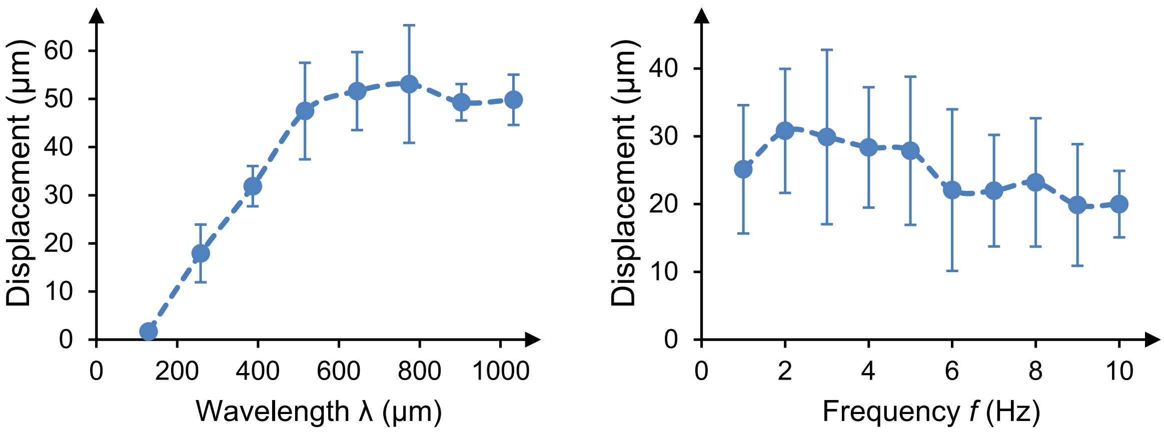

Figure S16. Wavelength- (left) and frequency-dependence (right) of the locomotion of a disk. In the wavelength analysis the frequency was set to 2 Hz and the average and standard deviation reported were estimated over 10 independent tests. In the frequency analysis the wavelength was fixed to 500 px (645 μm) and the average and standard deviation reported were estimated over 8 independent tests.

References

1 Thomsen, D. L. *et al.* Liquid Crystal Elastomers with Mechanical Properties of a Muscle. *Macromolecules* **34**, 5868-5875, doi:10.1021/ma001639q (2001).

2 Zeng, H. *et al.* High-Resolution 3D Direct Laser Writing for Liquid-Crystalline Elastomer Microstructures. *Advanced Materials* **26**, 2319-2322, doi:10.1002/adma.201305008 (2014).

3 García-Amorós, J. & Velasco, D. Recent advances towards azobenzene-based light-driven real-time information-transmitting materials. *Beilstein Journal of Organic Chemistry* **8**, 1003-1017, doi:10.3762/bjoc.8.113 (2012).

4 Garcia-Amorós, J., Finkelmann, H. & Velasco, D. Increasing the Isomerisation Kinetics of Azo Dyes by Chemical Bonding to Liquid-Crystalline Polymers. *Chemistry – A European Journal* **17**, 6518-6523, doi:10.1002/chem.201003453 (2011).

5 Davidson, P., Petermann, D. & Levelut, A., M. The Measurement of the Nematic Order Parameter by X-ray Scattering Reconsidered. *Journal de Physique II France* **5**, 113-131 (1995).

6 Sanchez-Castillo, A., Osipov, M. A. & Giesselmann, F. Orientational order parameters in liquid crystals: A comparative study of X-ray diffraction and polarized Raman spectroscopy results. *Physical Review E* **81**, 021707, doi:10.1103/PhysRevE.81.021707 (2010).

7 Warner, M. & Terentjev, E. M. *Liquid crystal elastomers*. Vol. 120 (Oxford University Press, 2003).

8 Zeng, H. *et al.* Light-Fueled Microscopic Walkers. *Advanced Materials* **27**, 3883-3887, doi:10.1002/adma.201501446 (2015).

9 Taylor, G. The Action of Waving Cylindrical Tails in Propelling Microscopic Organisms. *Proceedings of the Royal Society of London A: Mathematical, Physical and Engineering Sciences* **211**, 225-239, doi:10.1098/rspa.1952.0035 (1952).

10 Taylor, G. Analysis of the Swimming of Microscopic Organisms. *Proceedings of the Royal Society A: Mathematical, Physical and Engineering Sciences* **209**, 447-461, doi:10.1098/rspa.1951.0218 (1951).

11 Childress, S. Mechanics of swimming and flying. **2** (1981).